TOMOGRAPHIC MEASUREMENTS OF BAROTROPIC MOTIONS

by

Paul J. Bushong

B.S. Mechanical Engineering, United States Naval Academy, 1981

submitted in partial fulfillment of the
requirements for the dual degrees of

OCEAN ENGINEER
at the
MASSACHUSETTS INSTITUTE OF TECHNOLOGY
and the
WOODS HOLE OCEANOGRAPHIC INSTITUTION

and

MASTER OF SCIENCE IN OCEAN ENGINEERING
at the
MASSACHUSETTS INSTITUTE OF TECHNOLOGY
August, 1987

Signature of Author_____.
Department of Ocean Engineering, MIT and the
MIT–WHOI Joint Program in Oceanographic Engineering

Certified by_____.
Dr. John L. Spiesberger
Thesis Supervisor

Accepted by_____.
Dr. George V. Frisk
Chairman, Joint Committee for Oceanographic Engineering,
Massachusetts Institute of Technology–Woods Hole Oceanographic Institution

ABSTRACT

In 1983, continuous acoustic transmissions centered at 133 Hz and with a resolution of 60 ms were transmitted for five days from Oahu to the coast of Northern California (4000 km range). A maximum likelihood estimate of the change in acoustic travel time (based on phase) between received pulses is used to estimate barotropic fluctuations. Analysis of the resulting time series reveals resonant oscillations at nontidal frequencies in the Northeast Pacific. Some of the periods of the resonant oscillations are consistent with theory (Platzman, Curtis, Hansen, and Slater, 1981).

A Wiener filter is formulated for estimating the barotropic tides from a basin scale tomographic array. Error analyses indicate an ability to estimate barotropic currents and surface displacements with errors less than 0.01 cm/s and 1 cm, respectively, over a large portion of the Northeast Pacific.

ACKNOWLEDGEMENTS

I am indebted to my thesis advisor, John Spiesberger, for his guidance. Without his insight and suggestions, this thesis would not have been completed on time.

I would like to thank E.W. Schwiderski of the Naval Surface Weapons Center/ Dahlgren Laboratory for giving me his global ocean tide model and his hydrodynamical ocean depth data.

I am indebted to United States Navy for giving me the opportunity to pursue my graduate studies at MIT and WHOI.

Finally, I thank my wife, Dona, and my daughters, Cassandra and Sarah, for their love and support.

Contents

List of Figures

List of Tables

Chapter 1

Introduction

1.1 Motivation

There are many reasons to measure the large scale barotropic motions of the ocean. Some reasons are:

1. Basin scale barotropic motions which resonate in the world oceans have been theoretically predicted for simplified geometries by numerous investigators (eg. Lamb, 1932, Longuet-Higgins and Pond, 1970, and Pedlosky, 1987). Miller (1986) studied barotropic motions over variable topography in simplified basin shapes by numerically solving the shallow water equations for barotropic vorticity modes. Platzman (1979) developed a finite-element model of the world ocean which allows for topography and numerically solved for the barotropic normal modes predicting 56 modes with periods between 8 and 80 hours (Platzman, Curtis, Hansen, and Slater, 1981). Lacking from the studies of barotropic modes are direct observations. With ocean acoustic tomography, it is possible to measure the excited modes and gain insight into the forcing mechanisms, whether they be the wind (Luther, 1983) or the mesoscale eddy field (Miller, 1986).

2. Numerical tidal models with varying degrees of sophistication and assumptions (eg. Estes, 1977, Parke and Hendershott, 1980, and Schwiderski, 1978) exist, but are limited to a tidal height accuracy of 10 cm (Schwiderski, 1978) and give no estimates of the barotropic currents. Accurate estimates of surface elevation are useful in a number of applications including the determination of satellite orbits, mean sea surface computation (Marsh, Martin, McCarthy, and Chovitz, 1980), and satellite measurement of surface currents. With acoustic tomography, tidal height estimates are improved, and barotropic tidal current estimates are a direct result of the analysis.

1.2 Overview

In Chapter 2, we develop the maximum likelihood estimate of the tomographic travel time fluctuations due to barotropic motions. We apply this technique to five days of data from the acoustic tomography experiment of 1983 and perform spectral analysis on the resulting travel time series.

In Chapter 3, we formulate a Wiener filter to estimate the barotropic tides. Error maps based on synthetic data are shown.

Chapter 2

Measurement of Travel Time Changes Due to Barotropic Motions

The acoustic tomography experiment in 1983 (abbreviated to AT83) was conducted by Spiesberger, Metzger, and Birdsall and is the subject of two papers in preparation (Spiesberger, Bushong, Metzger, and Birdsall, 1987, and Spiesberger, Metzger, and Birdsall, 1987). We present a short description of the AT83 experiment, a method for measuring the tomographic travel time changes caused by barotropic motions, and the results of this analysis on the AT83 data.

2.1 Geometry and Signal Processing of the AT83 Experiment

The AT83 experiment consisted of approximately one week of acoustic transmissions between a bottom-mounted source at 183 meter depth on the coast of Oahu and a bottom-mounted receiver at mid-depth off the coast of California (Figure 2.1). The distance was about 4000 km. The transmitted signal had a center frequency of 133 Hz and a bandwidth of about 17 Hz. The source was not able to transmit a pulse which could be received above the noise at the receiver.

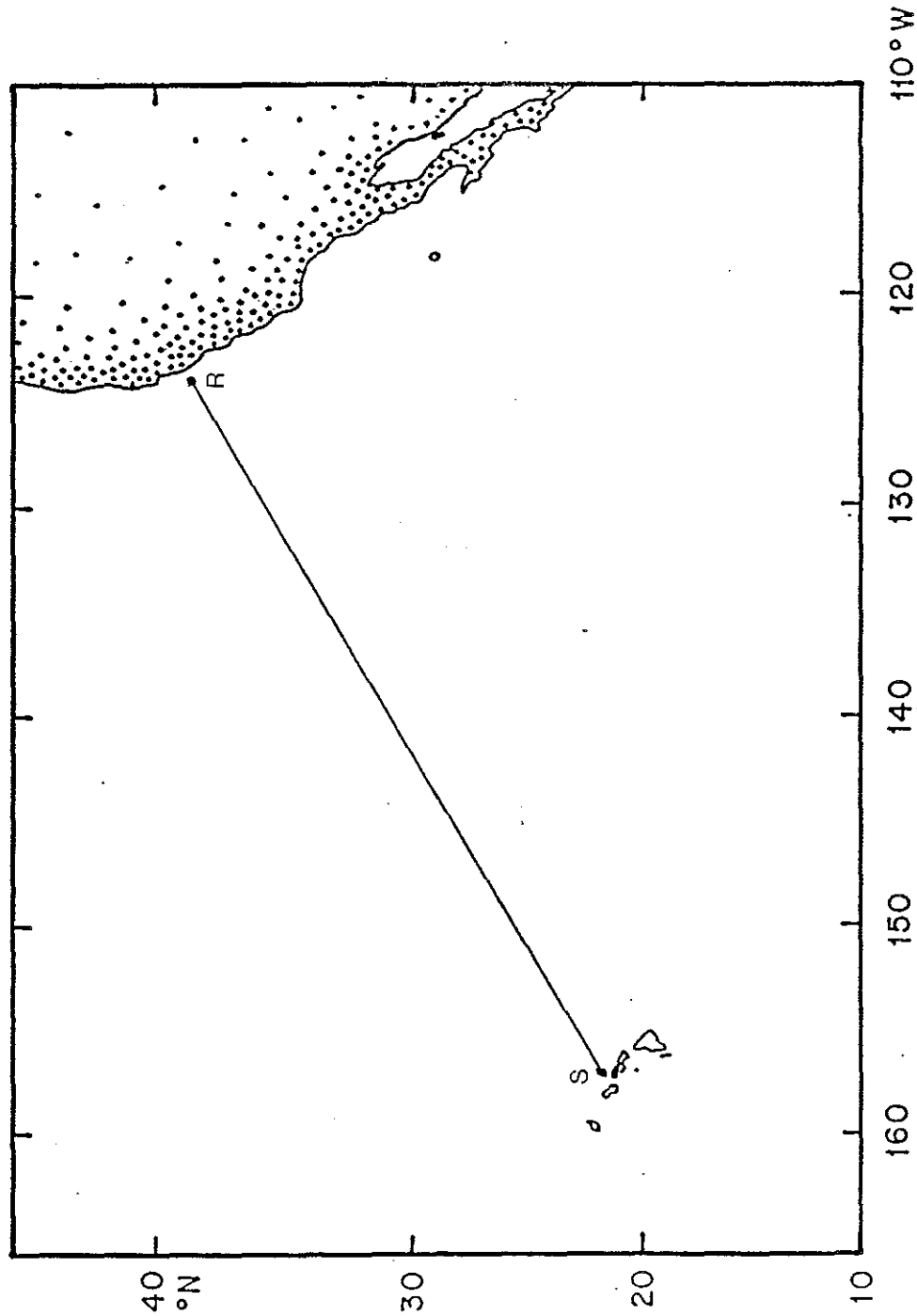

Figure 2.1: The acoustic tomography experiment in 1983 consisted of a source (S) located near Kaneohe Bay, Oahu, and a bottom-mounted receiver (R) whose approximate position is shown. The distance between the instruments was about 4000 km.

Instead, the 133 Hz signal was phase-modulated every 8 cycles using a 511 digit maximal shift register sequence having a period of $511(8/133) = 30.7$ seconds. Continuous transmissions were made between yeardays 333 (29 November) and 339 (5 December) in 1983 except for two gaps, one of 2 hours duration and the other of 5 hours duration.

The received signal was complex demodulated and correlated with a phase modulation replica (phase-only filtering). Replica correlation produced an output equivalent to the signal which would be received if a 60 ms pulse was transmitted every 30.7 seconds. This correlation also gave a signal-to-noise ratio increase of $10 \log_{10} 511 = 27$ dB along each ray path. Four successive pulse receptions were averaged together to increase the signal-to-noise ratio by an additional $10 \log_{10} 4 = 6$ dB and resulted in multipath records at two minute intervals. The final record was sampled at about 15 ms intervals (two cycles of carrier). A running average across four samples increased the signal-to-noise ratio by $10 \log_{10} 4 = 6$ dB with the loss of some resolution. These processing steps are identical to those used before (Spindel, 1979, and Spiesberger, Spindel, and Metzger, 1980) except for the specific frequencies, averaging intervals, and shift registers used.

Multipaths arrived over a four second interval. Adjacent acoustic records do not look similar because of the fluctuations of internal waves (Spiesberger, Metzger, and Birdsall, 1987). Incoherent averages over a period equal to the lowest internal wave period (about one cycle per day at this latitude) filter out much of the short term acoustic variability (Spiesberger, Spindel, and Metzger, 1980). Figure 2.2 shows the result of incoherently averaging 703 acoustic records (24 hours of data) on each of four days. There are five stable ray arrivals (A-E).

The time base of the signal generator on Oahu was maintained by a Rubidium oscillator and a GOES satellite receiver. The time at which the signal left the signal generator was measured to an accuracy of 1 ms. The signal travelled through

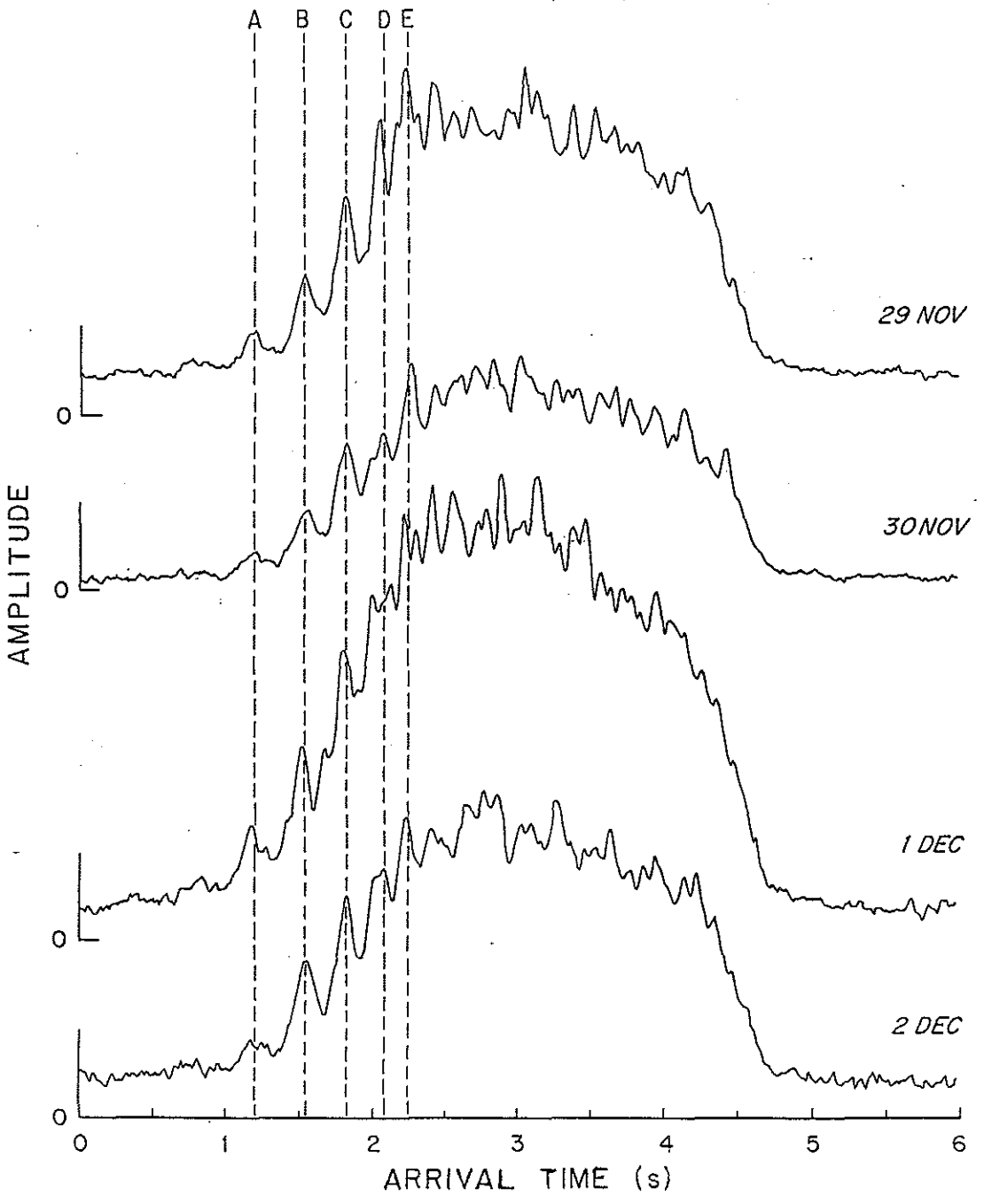

Figure 2.2: Incoherent averages of received pulses over 24 hours (703 pulsed transmitted at intervals of about 2 minutes). The 60 ms pulses transmitted at the Kaneohe source are spread by multipaths and arrive at the Northern California coast over an interval of about four seconds. Five stable ray arrivals (A-E) are indicated.

a power amplifier, a 5 mile length of cable, and through the acoustic source. The delay through the acoustic source is known to an accuracy of about 20 ms. Although the transmission time is only known to 20 ms, the change in transmission time was known to about 10 μs during the experiment.

The time base at the receiver was also maintained by a Rubidium oscillator and a GOES satellite receiver. The accuracy of the receiver clock was about 2 ms. The drift of this clock was less than 10 μs during the experiment.

Since the source and the receiver were bottom-mounted, acoustic travel time changes exceeding about 14 μs were due to ocean fluctuations or noise.

2.2 The Effect of Barotropic Motions on Tomographic Travel Times

The change in acoustic travel time along a ray path Γ_0 due to fluctuations in temperature, $\delta\theta$, sea surface displacement, η_0, and currents, $\vec{u}$, is given by,

$$\delta T(t) = -\alpha \int_{\Gamma_0} \frac{\delta\theta(\vec{x},t)}{c_0^2(\vec{x},t)} ds - k \int_{\Gamma_0} \frac{\eta_0(\vec{x},t)}{c_0^2(\vec{x},t)} ds - \int_{\Gamma_0} \frac{\vec{u}(\vec{x},t)\cdot\hat{s}}{c_0^2(\vec{x},t)} ds \qquad (2.1)$$

(Munk and Wunsch, 1978, and Munk, et al., 1981). The position along the ray path is $\vec{x}$, and the geophysical time is t. An increment along the ray path is ds and has a direction given by $\hat{s}$. The reference sound speed is denoted by c_0. Typical values for k and α are 0.017 s^{-1} and 4.785 $\frac{m}{^oC-s}$.

Barotropic fluctuations whose horizontal scale is much greater than a ray cycle distance (about 50 km) will affect all ray travel times about the same. The barotropic tides have large scales (order 1000 km). Typical values are,

$$\eta_0 \sim 1\,\text{meter}$$
$$u \sim 0.02\,\text{m/s}.$$

The associated isotherm displacement causes a temperature of about

$$\delta\theta \sim 0.005^{o}C$$

in the main thermocline. The ray will spend about one quarter of its time in the displaced thermocline. For a range of 4000 km, the magnitudes of the three terms in equation (2.1) are 10 ms, 30 ms, and 36 ms, respectively. In the next section we demonstrate that these perturbations are significant in comparison with the uncertainty of our travel time measurements.

2.3 Measurement of Travel Time Change Using Phase

We seek a method of estimating the average travel time change between records in order to search for large scale barotropic processes. Travel time measurements based on phase are usually more accurate than those based on amplitude.

Acoustic travel time changes appear as changes in the phase of the demodulated complex signal; the travel time change, τ, being linearly related to the phase, ϕ, through $\phi = \omega\tau$ where ω is the carrier frequency. Measured phase is a modulo 1 cycle process. Ambiguities may result when extending the phase past one cycle (Dyson, Munk, and Zetler, 1976).

The $1/e$ decorrelation time of the complex cross correlation for our records is 4.3 minutes (Figure 2.3). We can use the high correlation of adjacent acoustic signals (separated by two minutes) to estimate the average change in phase. The two adjacent complex records can be written as,

$$r_1(t) = f_1(t)\exp\left[j(\omega_c t + \phi_1 + \theta(t))\right] \tag{2.2}$$

$$r_2(t) = f_2(t)\exp\left[j(\omega_c t + \phi_2 + \theta(t))\right], \tag{2.3}$$

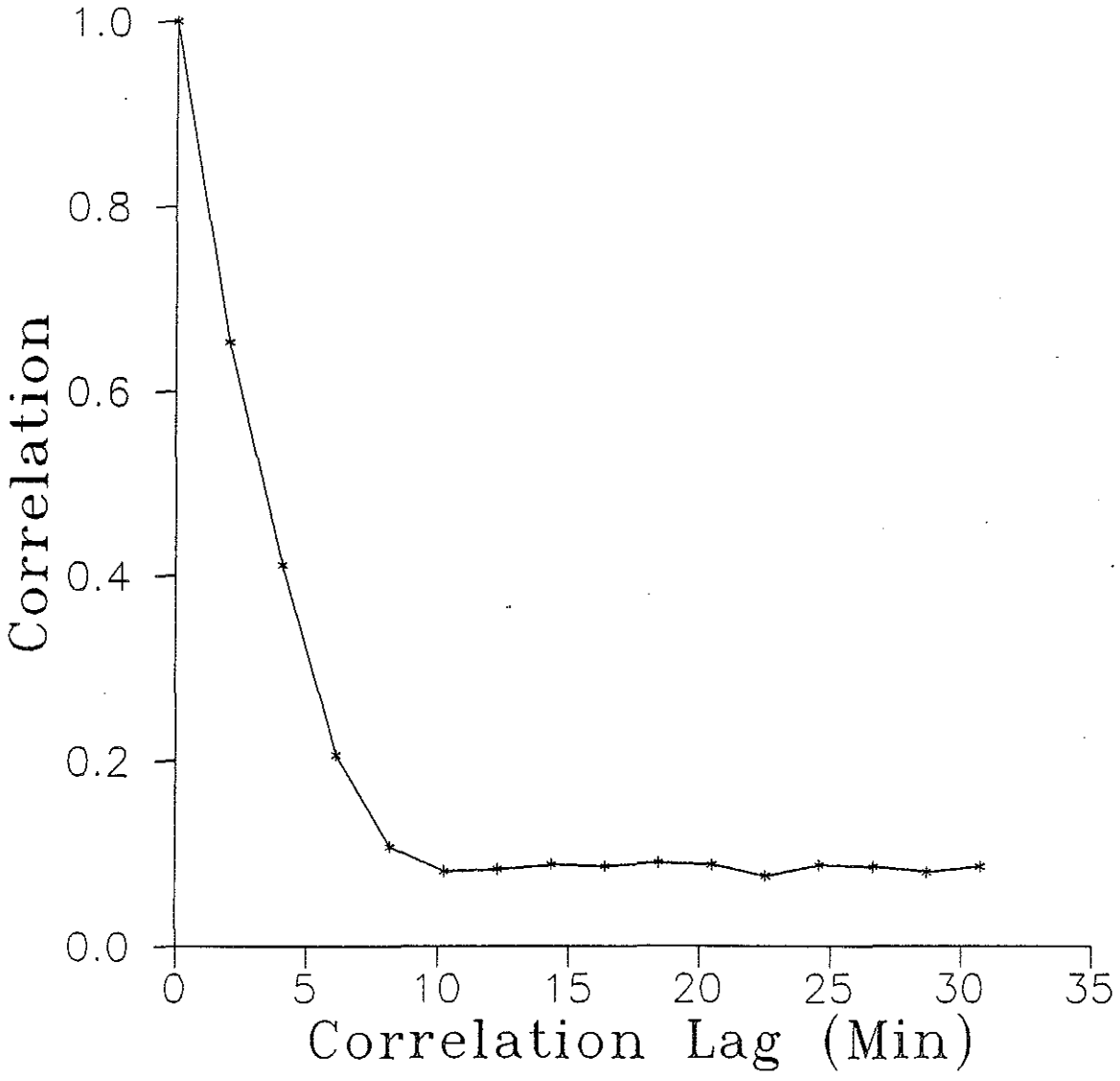

Figure 2.3: Peak cross correlation magnitudes versus transmission time separation indicate a 1/e decorrelation time of 4.3 minutes. Each point is an average across ten realizations.

where $f_1(t)$ and $f_2(t)$ are non-negative valued functions, $\phi_2 - \phi_1$ is the average change in phase, and $\theta_1(t)$ and $\theta_2(t)$ account for the other phase fluctuations. We wish to estimate the change in the average phase, $\Delta\phi_2 = \phi_2 - \phi_1$ every two minutes. The sufficient statistics X and Y, defined as,

$$X = Re\left\{\frac{1}{\delta t}\int_0^{\delta t} r_1(t)r_2^*(t)dt\right\} \tag{2.4}$$

$$Y = jIm\left\{\frac{1}{\delta t}\int_0^{\delta t} r_1(t)r_2^*(t)dt\right\}, \tag{2.5}$$

where $*$ indicates the complex conjugate, lead to the maximum likelihood (matched filter) estimate of the phase change,

$$\Delta\phi = \arctan\left(\frac{Y}{X}\right) \tag{2.6}$$

(Van Trees, 1968). The upper limit of integration of equations (2.4) and (2.5), δt, is chosen to include only the incoming signals. The unwrapped or extended phase is then,

$$\phi_n = \phi_{n-1} + \Delta\phi_n, \tag{2.7}$$

where the subscript n indicates the record number, and an initial phase, ϕ_1, of zero is assumed. We call this matched filter processing because the filtering of the second signal is matched to the previous signal.

Previous continuous wave (CW) experiments have estimated travel time fluctuations from the means of the real and imaginary parts of the complex demodulated signal. If $x(t)$ and $y(t)$ are the real and imaginary parts of the complex demodulated signal, respectively, and δt is the averaging period, the estimates of the means are,

$$X(t) = \frac{1}{\delta t}\int_0^{\delta t} x(t)dt \tag{2.8}$$

$$Y(t) = \frac{1}{\delta t}\int_0^{\delta t} y(t)dt, \tag{2.9}$$

with a phase estimate of

$$\phi(t) = \arctan\left(\frac{Y(t)}{X(t)}\right). \tag{2.10}$$

Difficulty arises in extending the modulo 1 cycle phase when the phase changes are large.

The first two days of the AT83 experiment data were processed using both methods (Figure 2.4). CW processing was performed by calculating $X(t)$ and $Y(t)$ according to equations (2.8) and (2.9). The limit of integration, δt, was four seconds to include only the signal. Phase was extended according to,

$$|\phi_n - 1/2(\phi_{n-1} + \phi_{n-2})| < 1/2\,\text{cycle}. \tag{2.11}$$

Phase kinks were then removed according to,

$$|\phi_n - 1/2(\phi_{n+1} + \phi_{n-1})| < 1/2\,\text{cycle} \tag{2.12}$$

(Dyson, Munk, and Zetler, 1976). The long-period divergence of the estimators is caused by the ambiguity of extending the CW record after large phase changes. Figure 2.5 shows histograms of CW and matched filter phase change over two minutes for five days of data. The large phase changes in the CW record can be attributed to the integration processes of equations (2.8) and (2.9) which are sensitive to any multipath fading.

2.4 Observations of Resonant Oscillations in the Northeast Pacific

We use spectral analysis to investigate the estimates of travel time (Figures 2.6 and 2.7) over the first five days of the AT83 experiment. All spectral estimates are one-sided. A line fit was used to detrend the travel time series. The trend

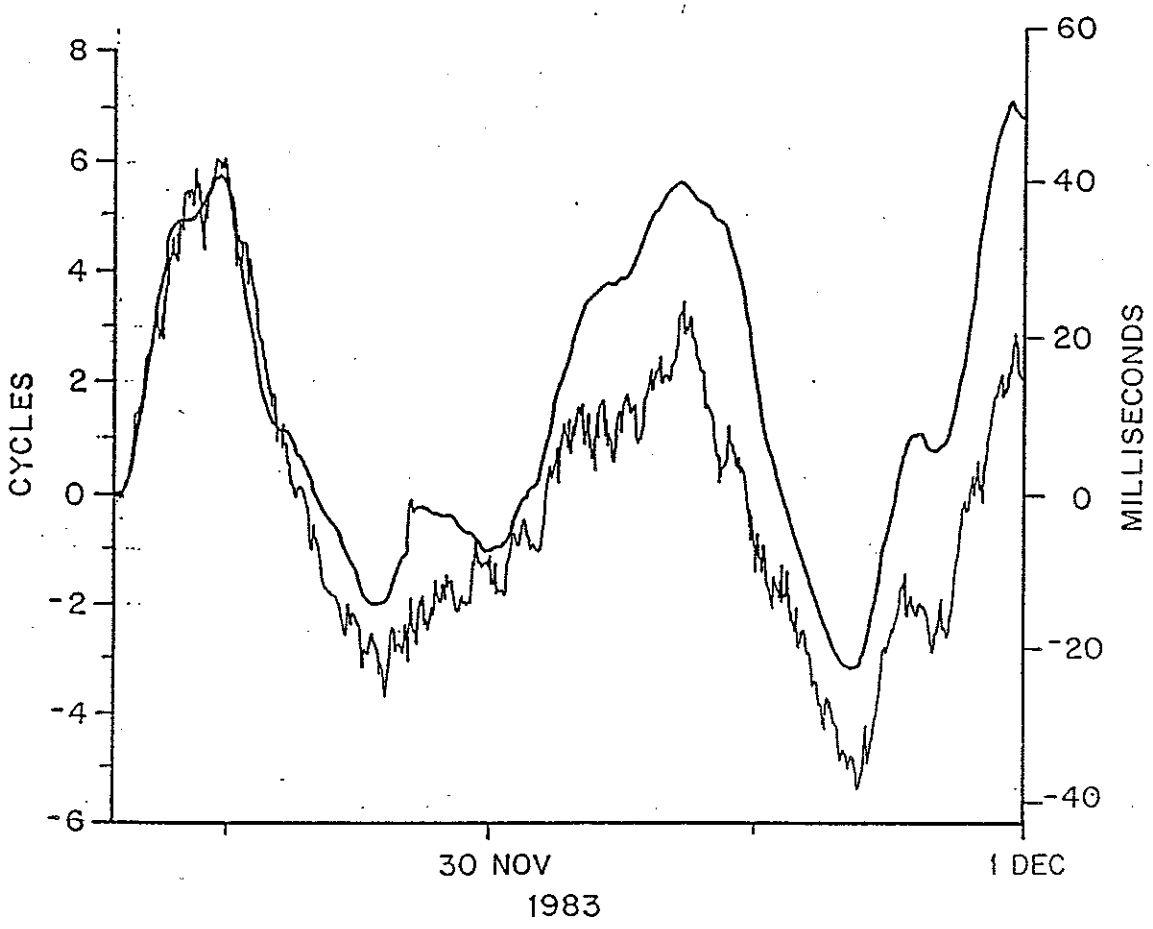

Figure 2.4: Two estimators of the acoustic travel time change (one phase cycle is about 7 ms) based on phase from two day of data. The jagged curve is the estimate obtained if the source transmitted a CW signal at 133 Hz where phase is unwrapped according to equations (2.11) and (2.12). The smooth curve is the estimate obtained with matched filter processing. The long-period divergence of the estimators is caused by the ambiguity of unwrapping the CW record after large phase changes.

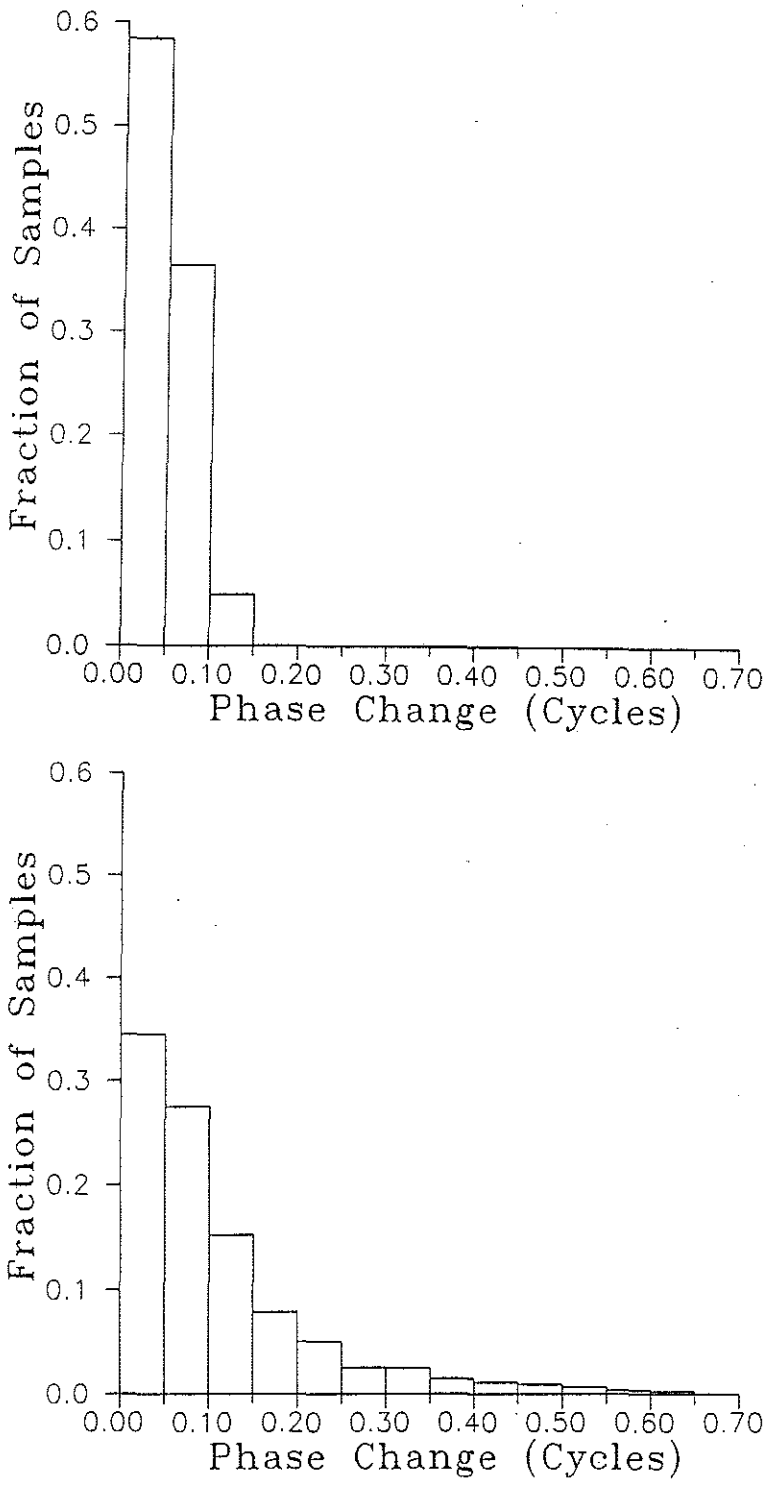

Figure 2.5: Histograms of the measured phase change in two minutes over five days of data (3486 records) using:
Top: Matched filter processing
Bottom: CW processing.

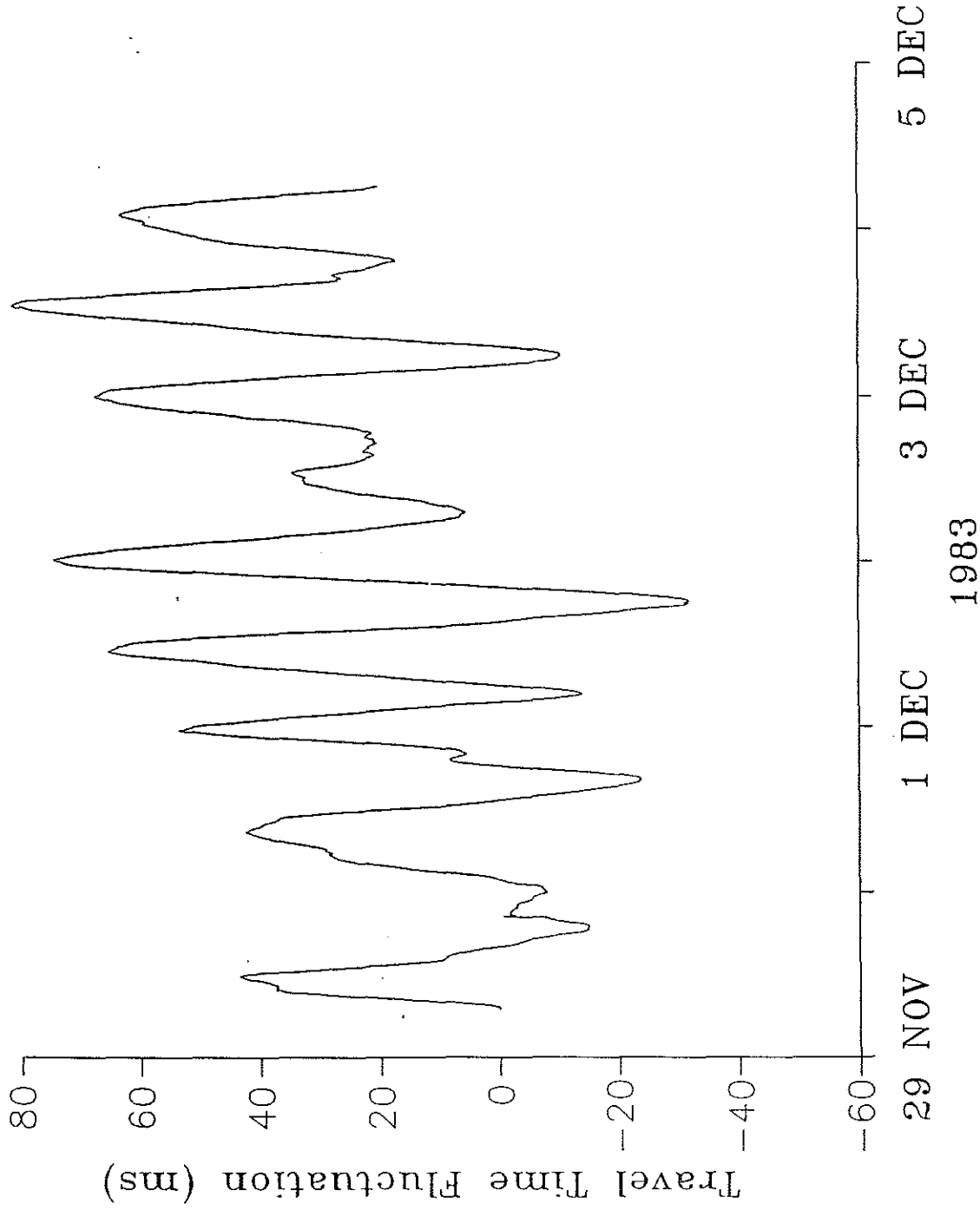

Figure 2.6: The matched filter processing used to estimate the acoustic travel time change over 4000 km from the Kaneohe source near Oahu to the Northern California coast.

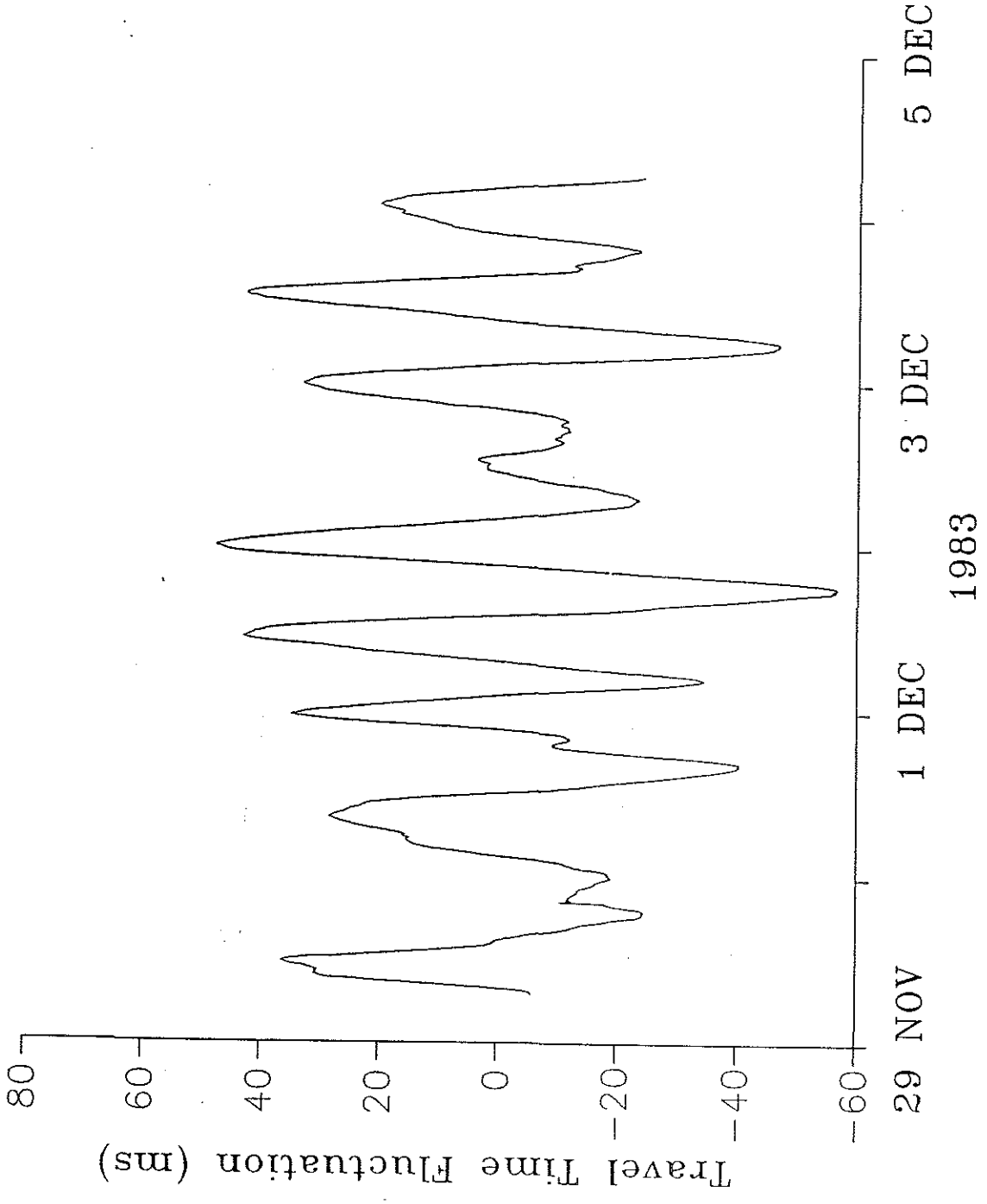

Figure 2.7: Acoustic travel time change of Figure 2.6 detrended by a line fit. Over the five day series, the trend accounts for a travel time increase of 38 ms corresponding to a cooling of the Northeast Pacific.

Spectral Technique	Peak Number	Period (hr)	Variance (cycles^2)
Periodogram	1	20.7	1.8
Autoregressive	1	21.2	1.7
Prony	1	21.4	1.3
Periodogram	2	15.8	1.6
Autoregressive	2	15.5	2.4
Prony	2	15.7	3.7
Periodogram	3	12.2	5.0
Autoregressive	3	12.3	6.0
Prony	3	12.3	4.3
Periodogram	4	9.8	—
Autoregressive	4	9.6	—
Prony	4	9.4	1.5

Table 2.1: A summary of the prominent peaks from three spectral estimates of the travel time series of Figure 2.7

accounted for a 38 ms increase in acoustic travel time corresponding to a cooling of the Northeast Pacific.

We use three spectral estimators to measure the frequencies of variation of the travel time series; a periodogram (Figure 2.8), the autoregressive method (Figure 2.9), and Prony's method (Figure 2.10). The periodogram is a classical spectral technique which is robust for long, wide-sense stationary series, but is limited by sidelobes and resolution for short series. Autoregressive and Prony's method are more suitable for short series because they have high resolution without sidelobes (Kay and Marple,1981, and Marple, 1987).

We discuss four peaks which all three spectral estimators exhibit (Table 2.1). Four observations are made:

1. The diurnal tide peak which is expected at a period of about 24 hours is not present. A peak at a period near 21.2 hours exists.

2. A peak occurs at a period of 15.7 hours.

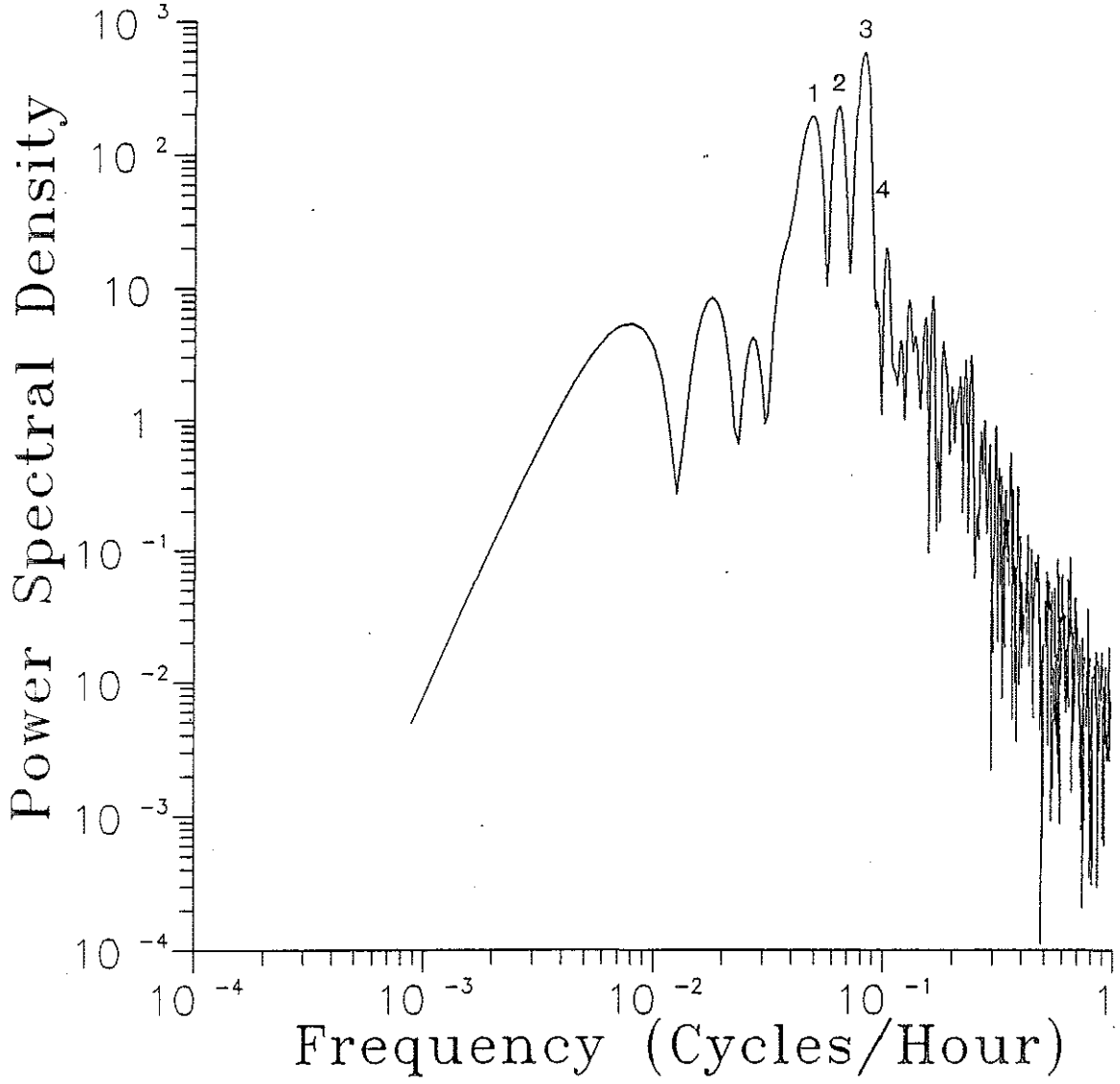

Figure 2.8: Periodogram estimate of the power spectral density (cycles^2/cph) of the detrended phase series (Figure 2.7). The three major peaks occur at periods of 20.7, 15.8, and 12.2 hours.

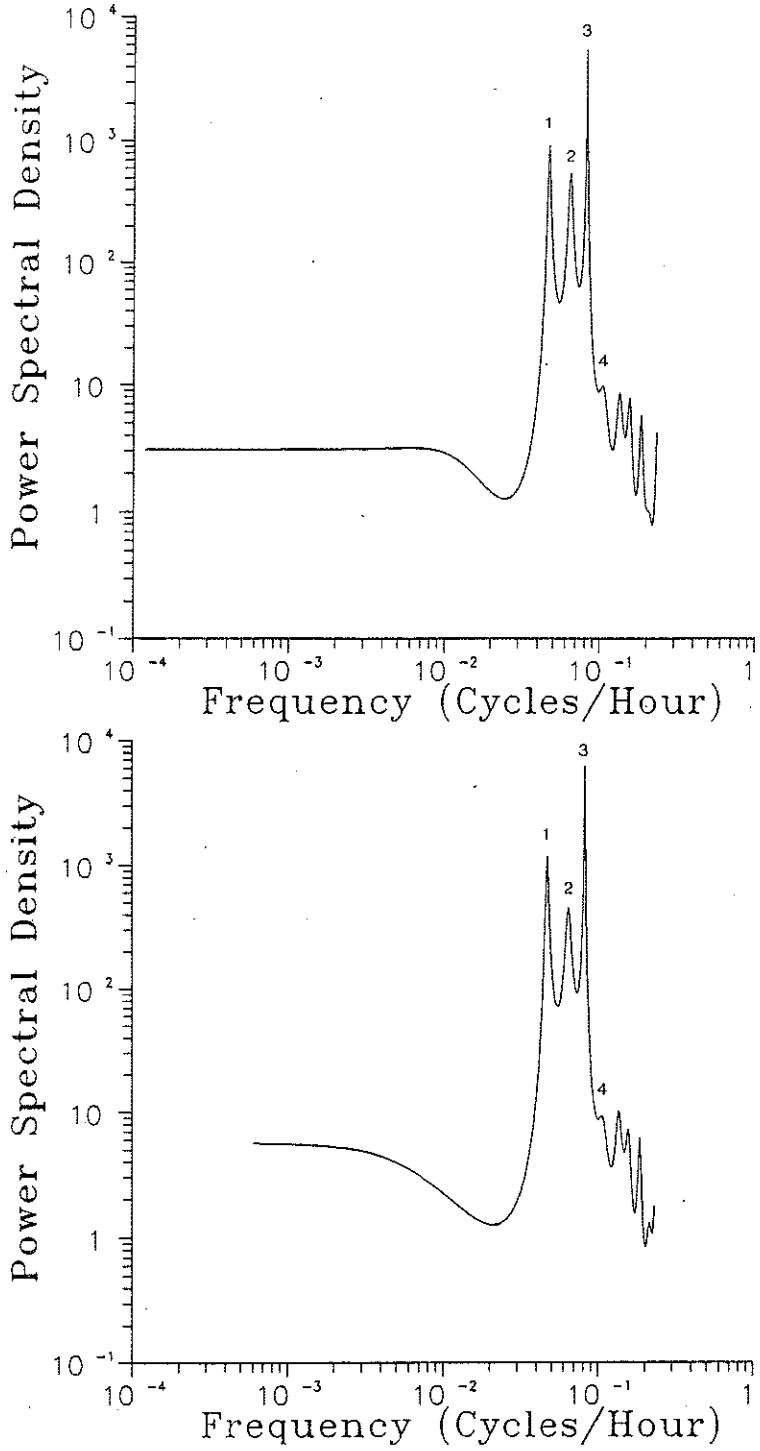

Figure 2.9: Autoregressive method estimates of the power spectral density (cycles^2/cph) of the detrended phase series (Figure 2.7).
Top: Sample lags of 30.7 min and a model order of 75.
Bottom: Sample lags of 6.1 min and a model order of 400.
In both estimates, the major peaks occur at periods of 21.2, 15.5, and 12.3 hours.

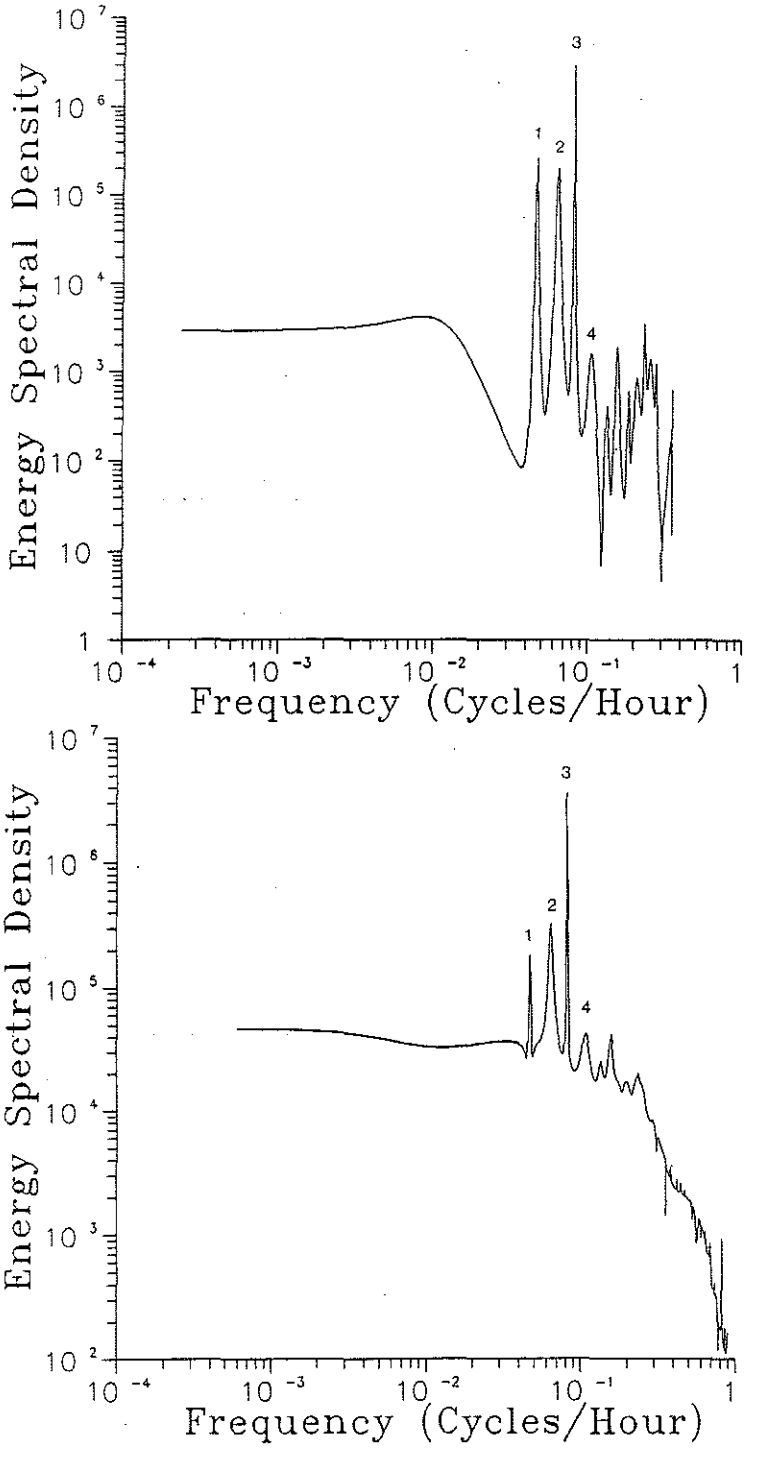

Figure 2.10: Prony's method estimates of the energy spectral density (cycles^2/cph^2) of the detrended phase series (Figure 2.7).
Top: Sample lags of 30.7 min and a model order of 75.
Bottom: Sample lags of 6.1 min and a model order of 400.
In both estimates, the major peaks occur at periods of 21.4, 15.7, and 12.3 hours.

Mode Number	Period (hr)	Mode Description
16	28.7	Pacific 1/2 wave; Antarctic Kelvin wave 1
19	21.2	Pacific 2/2 wave
25	15.5	Pacific North American Kelvin wave
26	15.2	Antarctic Kelvin wave 2
32	12.5	Arabian Sea; North Pacific
35	11.6	Equatorial Pacific transverse 3/2 wave
46	9.2	Equatorial Pacific transverse 4/2 wave

Table 2.2: Predicted barotropic normal modes of the Northeast Pacific with periods between 9 and 30 hours (from Platzman, Curtis, Hansen, and Slater, 1981).

3. The semi-diurnal tide peak which is expected near a period of 12 hours is present.

4. A smaller, but significant, peak appears at a period of 9.2 hours.

In seeking to explain these results, we cite the work of Platzman (Platzman, 1979, and Platzman, Curtis, Hansen, and Slater, 1981). He developed a barotropic finite-element model of the world ocean which allowed for topography and numerically solved for the barotropic normal modes, finding 56 modes with periods between 8 and 80 hours. Of these 56 modes, 41 have periods between 8 and 30 hours and are primarily gravity modes, that is, gravity provides the restoring force. A listing of some of Platzman's normal modes with periods between 9 and 25 hours is given in Table 2.2.

The spectral peaks at periods of 21.2, 15.5, and 9.2 hours correspond to Platzman's modes. The phase series length is insufficient to resolve both the 15.2 and 15.5 hour period components. Other significant peaks appear in all three spectral estimators (periods of 7.5, 6.4, and 5.3 hours) but have periods less than those computed by Platzman.

Chapter 3

Estimation of Barotropic Tides

We formulate an inversion filter to estimate the barotropic tides. The periodic barotropic motions are required to satisfy conservation of mass and are specified by four current models. The earth is assumed to be spherical, and vertical displacements are relative to the earth's surface. Root mean square estimation errors are explored for a source-receiver array similar to that of the acoustic tomography experiment of 1986-87.

3.1 Forward Problem

The change in acoustic travel time along a ray path Γ_0 due to isotherm displacement, η, surface displacement, η_0, and currents, $\vec{u}$, follows from equation (2.1) and is given by,

$$\delta T(t) = -\frac{1}{\tilde{c}^2}\int_{\Gamma_0}\left[k\eta_0(\vec{x},t) + \vec{u}(\vec{x},t)\cdot\hat{s} + \frac{\partial c_p(\vec{x},t)}{\partial z}\eta(\vec{x},t)\right]ds, \qquad (3.1)$$

where $\partial c_p/\partial z$ is the potential sound speed gradient (Munk, et al.,1981) and $z = r_0 - r$ where r_0 is the earth's radius. A representative value of sound speed, $\tilde{c}$, has been substituted for the position dependent sound speed.

The barotropic current as a function of colatitude, θ, longitude (east), ϕ, frequency, ω, and time, t, is taken to be,

$$\begin{aligned}\vec{u}(\theta,\phi,\omega,t) &= [a_1(\theta,\phi,\omega)\cos\omega t + a_2(\theta,\phi,\omega)\sin\omega t]\,\hat{\theta} \\ &\quad + [b_1(\theta,\phi,\omega)\cos\omega t + b_2(\theta,\phi,\omega)\sin\omega t]\,\hat{\phi}. \end{aligned} \tag{3.2}$$

Surface elevation and currents are related through the continuity of mass equation,

$$\frac{\partial \eta_0(\vec{x},t)}{\partial t} = -\nabla_H \cdot (h(\vec{x})\vec{u}(\vec{x},t))\,, \tag{3.3}$$

where h is the ocean depth (positive) and ∇_H is the horizontal component of the gradient. Substituting equation (3.2) into equation (3.3) and integrating with respect to time gives,

$$\begin{aligned}&\eta_0(\theta,\phi,\omega,t) = \\ &\quad -\frac{1}{r\omega}\left[ha_1\cot\theta + ha_{1\theta} + hb_{1\phi}\csc\theta + h_\theta a_1 + h_\phi b_1\csc\theta\right]\sin\omega t \\ &\quad +\frac{1}{r\omega}\left[ha_2\cot\theta + ha_{2\theta} + hb_{2\phi}\csc\theta + h_\theta a_2 + h_\phi b_2\csc\theta\right]\cos\omega t, \end{aligned} \tag{3.4}$$

where the subscripts θ and ϕ indicate the derivative with respect to colatitude and longitude.

To relate the depth dependent vertical displacement to currents, we start with the continuity equation in terms of spherical component velocities, u, v, and w,

$$\frac{\partial w}{\partial r} + \frac{2w}{r} + \frac{1}{r\sin\theta}\left[v\sin\theta\right]_\theta + \frac{1}{r\sin\theta}u_\phi = 0. \tag{3.5}$$

From equation (3.2),

$$v = a_1\cos\omega t + a_2\sin\omega t \tag{3.6}$$

$$u = b_1\cos\omega t + b_2\sin\omega t. \tag{3.7}$$

Substituting these expressions into equation (3.5) and solving the differential equation with the boundary condition of zero normal flow at the bottom gives the

vertical velocity as a function of position and time. Integrating with respect to time gives the depth dependent vertical displacement as a function of position, frequency, and time,

$$\begin{aligned}\eta(\theta,\phi,z,\omega,t) = \\ &-\frac{1}{r\omega}\left[(h-z)(a_1\cot\theta + a_{1\theta} + b_{1\phi}\csc\theta) + h_\theta a_1 + h_\phi b_1 \csc\theta\right]\sin\omega t \\ &+\frac{1}{r\omega}\left[(h-z)(a_2\cot\theta + a_{2\theta} + b_{2\phi}\csc\theta) + h_\theta a_2 + h_\phi b_2 \csc\theta\right]\cos\omega t \quad (3.8)\end{aligned}$$

where z is positive downwards with $z = 0$ at the mean surface. The depth independent portion of equation (3.8) is the surface displacement, $\eta_0(\vec{x},t)$. Substituting equation (3.8) into equation (3.1) gives the frequency and time dependent travel time fluctuation,

$$\begin{aligned}\delta T(t,\omega) &= -\frac{1}{\tilde{c}^2}\int_{\Gamma_0}\left(k - \frac{\partial c_p(\vec{x},t)}{\partial z}\right)\eta_0(\vec{x},t)ds - \frac{1}{\tilde{c}^2}\int_{\Gamma_0}\vec{u}(\vec{x},t)\cdot\hat{s}\,ds \\ &+\frac{1}{\tilde{c}^2 r\omega}\int_{\Gamma_0}\left(z\frac{\partial c_p(\vec{x},t)}{\partial z}\right)(a_1\cot\theta + a_{1\theta} + b_{1\phi}\csc\theta)\sin\omega t\,ds \\ &-\frac{1}{\tilde{c}^2 r\omega}\int_{\Gamma_0}\left(z\frac{\partial c_p(\vec{x},t)}{\partial z}\right)(a_2\cot\theta + a_{2\theta} + b_{2\phi}\csc\theta)\cos\omega t\,ds. \quad (3.9)\end{aligned}$$

Evaluation of equation (3.9) requires path integration along single rays. We remove this requirement by approximating equation (3.9) with an integral in the horizontal only by assuming that the path integrals and horizontal integrals can be related through constants of proportionality so that,

$$\begin{aligned}\delta T(t,\omega) &= -\frac{1}{\tilde{c}^2}\left(k\gamma - \overline{\frac{\partial c_p}{\partial z}}\right)\int\eta_0(\vec{x},t)dl - \frac{1}{\tilde{c}^2}\int\vec{u}(\vec{x},t)\cdot\hat{s}\,dl \\ &+\frac{1}{\tilde{c}^2 r\omega}\left(\overline{z\frac{\partial c_p}{\partial z}}\right)\int(a_1\cot\theta + a_{1\theta} + b_{1\phi}\csc\theta)\sin\omega t\,dl \\ &+\frac{1}{\tilde{c}^2 r\omega}\left(\overline{z\frac{\partial c_p}{\partial z}}\right)\int(a_2\cot\theta + a_{2\theta} + b_{2\phi}\csc\theta)\cos\omega t\,dl, \quad (3.10)\end{aligned}$$

where,

$$\gamma \equiv \frac{\int_{\Gamma_0} ds}{\int dl} \quad (3.11)$$

$$\overline{\frac{\partial c_p}{\partial z}} \equiv \frac{\int_{\Gamma_0} \frac{\partial c_p(\vec{x},t)}{\partial z} ds}{\int dl} \tag{3.12}$$

$$\overline{z\frac{\partial c_p}{\partial z}} \equiv \frac{\int_{\Gamma_0} z\frac{\partial c_p(\vec{x},t)}{\partial z} ds}{\int dl}, \tag{3.13}$$

and dl is the increment in range along the transmission path. For notational convenience, we define,

$$c_1 = k\gamma - \overline{\frac{\partial c_p}{\partial z}} \tag{3.14}$$

$$c_2 = \overline{z\frac{\partial c_p}{\partial z}}, \tag{3.15}$$

and $\delta(\vec{x})$ equals the bearing to the receiver at any position, $\vec{x}$, along the transmission path. We substitute equations (3.2) and (3.4) into equation (3.10) to get the travel time fluctuation as a function of time and frequency,

$$\delta T_i(t,\omega) = e_i(\omega)\cos\omega t + f_i(\omega)\sin\omega t, \tag{3.16}$$

where,

$$\begin{aligned} e_i(\omega) &= -\frac{1}{\tilde{c}^2 r\omega}\int\{(c_1 h + c_2)(a_2\cot\theta + a_{2\theta} + b_{2\phi}\csc\theta) + c_1(h_\theta a_2 + h_\phi b_2\csc\theta)\}dl_i \\ &\quad + \frac{1}{\tilde{c}^2}\int(a_1\cos\delta - b_1\sin\delta)dl_i \end{aligned} \tag{3.17}$$

$$\begin{aligned} f_i(\omega) &= +\frac{1}{\tilde{c}^2 r\omega}\int\{(c_1 h + c_2)(a_1\cot\theta + a_{1\theta} + b_{1\phi}\csc\theta) + c_1(h_\theta a_1 + h_\phi b_1\csc\theta)\}dl_i \\ &\quad + \frac{1}{\tilde{c}^2}\int(a_2\cos\delta - b_2\sin\delta)dl_i, \end{aligned} \tag{3.18}$$

and the subscript i indicates the source-receiver pair. In this formulation of the forward problem, the data are $e_i(\omega)$ and $f_i(\omega)$ and are linearly related to the models, $a_1(\theta,\phi,\omega)$, $a_2(\theta,\phi,\omega)$, $b_1(\theta,\phi,\omega)$, and $b_2(\theta,\phi,\omega)$ as in equations (3.17) and (3.18).

3.2 Inverse Problem

We have chosen to use a Wiener filter to estimate the models (Cornuelle, 1983, The Ocean Tomography Group, 1982). With N transmission paths, the $2N \times 1$ data vector,

$$\vec{d}(\omega) = [e_1(\omega)\ f_1(\omega)\ e_2(\omega)\ f_2(\omega) \ldots e_N(\omega)\ f_N(\omega)]^T, \tag{3.19}$$

is formed from the travel time coefficients of equation (3.16).

The $2N \times 2N$ data-data covariance matrix,

$$D'(\omega) = E\left[\vec{d}(\omega)\vec{d}^T(\omega)\right], \tag{3.20}$$

and the $2N \times 1$ model-data covariance vectors,

$$\begin{aligned}
\vec{\beta}_{a_1}(\theta,\phi,\omega) &= E(\vec{d}\,a_1(\theta,\phi,\omega)) \\
\vec{\beta}_{a_2}(\theta,\phi,\omega) &= E(\vec{d}\,a_2(\theta,\phi,\omega)) \\
\vec{\beta}_{b_1}(\theta,\phi,\omega) &= E(\vec{d}\,b_1(\theta,\phi,\omega)) \\
\vec{\beta}_{b_2}(\theta,\phi,\omega) &= E(\vec{d}\,b_2(\theta,\phi,\omega)),
\end{aligned} \tag{3.21}$$

can be computed from equations (3.17) and (3.18) given the auto-correlation and cross-correlation functions of a_1, a_2, b_1, and b_2. Each element of the data-data covariance matrix requires a double integral over two transmission paths while each element of the model-data covariance vectors requires an integral over one transmission path. The computed data-data covariance matrix, $D'(\omega)$ is augmented by a noise covariance matrix, $D_N(\omega)$, to account for noise in the data vector, $\vec{d}$, and to account for approximations the forward problem. The total data-data covariance matrix, $D(\omega)$, is given by,

$$D(\omega) = D'(\omega) + D_N(\omega). \tag{3.22}$$

The discrete Wiener filter or stochastic inverse estimate of $a_1(\theta,\phi,\omega)$ is given by,

$$\hat{a_1}(\theta,\phi,\omega) = \vec{\beta}_{a_1}(\theta,\phi,\omega)D^{-1}(\omega)\vec{d}(\omega), \tag{3.23}$$

and has a mean square estimation error of

$$E\left[(a_1(\theta,\phi,\omega) - \hat{a_1}(\theta,\phi,\omega))^2\right] = E\left[(a_1(\theta,\phi,\omega))^2\right] - \vec{\beta}^T_{a_1}(\theta,\phi,\omega)D^{-1}(\omega)\vec{\beta}_{a_1}(\theta,\phi,\omega) \tag{3.24}$$

(Kailath, 1981, and Aki and Richards, 1980). Substituting the appropriate model-data covariance vector gives similar expressions for $\hat{a_2}$, $\hat{b_1}$, and $\hat{b_2}$.

Estimates of the surface displacement, η_0, follow directly from equation (3.4) and are given by,

$$\begin{aligned}\hat{\eta_0}(\theta,\phi,\omega,t) = & \\ & -\frac{1}{r\omega}\left[h\hat{a_1}\cot\theta + h\hat{a_{1\theta}} + h\hat{b_{1\phi}}\csc\theta + h_\theta\hat{a_1} + h_\phi\hat{b_1}\csc\theta\right]\sin\omega t \\ & +\frac{1}{r\omega}\left[h\hat{a_2}\cot\theta + h\hat{a_{2\theta}} + h\hat{b_{2\phi}}\csc\theta + h_\theta\hat{a_2} + h_\phi\hat{b_2}\csc\theta\right]\cos\omega t. \end{aligned} \tag{3.25}$$

The mean square error of this estimate is

$$E\left[(\eta_0 - \hat{\eta_0})^2\right] = E\left[\eta_0^2\right] - E\left[\eta_0\hat{\eta_0}\right], \tag{3.26}$$

where $E[\eta_0^2]$ is the *a-priori* variance of the surface displacement. The reduction in variance, $E[\eta_0\hat{\eta_0}]$, follows from equations (3.4), (3.21), and (3.25) and is given by,

$$E\left[\eta_0\hat{\eta_0}\right] = \frac{1}{(r\omega)^2}\vec{\alpha}^T(\omega)D^{-1}(\omega)\vec{\alpha}(\omega), \tag{3.27}$$

where

$$\vec{\alpha}(\omega) = (h_\theta + h\cot\theta)\vec{\beta}_{a_2}(\omega) + h\frac{\partial\vec{\beta}_{a_2}(\omega)}{\partial\theta} + h_\phi\csc\theta\vec{\beta}_{b_2}(\omega) + h\csc\theta\frac{\partial\vec{\beta}_{b_2}(\omega)}{\partial\phi}. \tag{3.28}$$

3.3 Error Analysis

The acoustic tomography experiment of 1986-87 (AT86-87) consisted of three deep ocean tethered sources, one source near Kaneohe Bay, Oahu, and about ten bottom mounted receivers. The area covered by the array was about 4000 km x 3000 km. To explore the ability of the inversion filter to account for the *a-priori* variances of the currents and surface displacements, we choose a source-receiver array with four sources that correspond to those of the AT86-87 experiment but with only five receivers (Figure 3.1). The area covered by this array is similar to that of the AT86-87 experiment, but with less resolution.

We assume that the current components are statistically independent and that the autocorrelation function of each current component is Gaussian and a function only of the distance, X, between the two geographic points. That is,

$$\begin{aligned} E\left[a_1(\theta_1,\phi_1,\omega)a_1(\theta_2,\phi_2,\omega)\right] &= \sigma^2 \exp\left(-\frac{X^2}{L^2}\right) \\ E\left[a_2(\theta_1,\phi_1,\omega)a_2(\theta_2,\phi_2,\omega)\right] &= \sigma^2 \exp\left(-\frac{X^2}{L^2}\right) \\ E\left[b_1(\theta_1,\phi_1,\omega)b_1(\theta_2,\phi_2,\omega)\right] &= \sigma^2 \exp\left(-\frac{X^2}{L^2}\right) \\ E\left[b_2(\theta_1,\phi_1,\omega)b_2(\theta_2,\phi_2,\omega)\right] &= \sigma^2 \exp\left(-\frac{X^2}{L^2}\right), \end{aligned} \tag{3.29}$$

and,

$$E[a_1a_2] = E[a_1b_1] = E[a_1b_2] = E[a_2b_1] = E[a_2b_2] = E[b_1b_2] = 0, \tag{3.30}$$

where σ^2 is the variance of a_1, a_2, b_1, and b_2, and L is the 1/e decorrelation length.

A decorrelation length of 1500 km is assumed, and all error analyses are computed for a frequency equal to that of the M2 tidal component. The *a-priori* variance on each current model is taken to 1.0 cm^2/s^2 to give an *a-priori* error of the current magnitude of 2.0 cm/s, typical of the magnitude of the M2 tidal

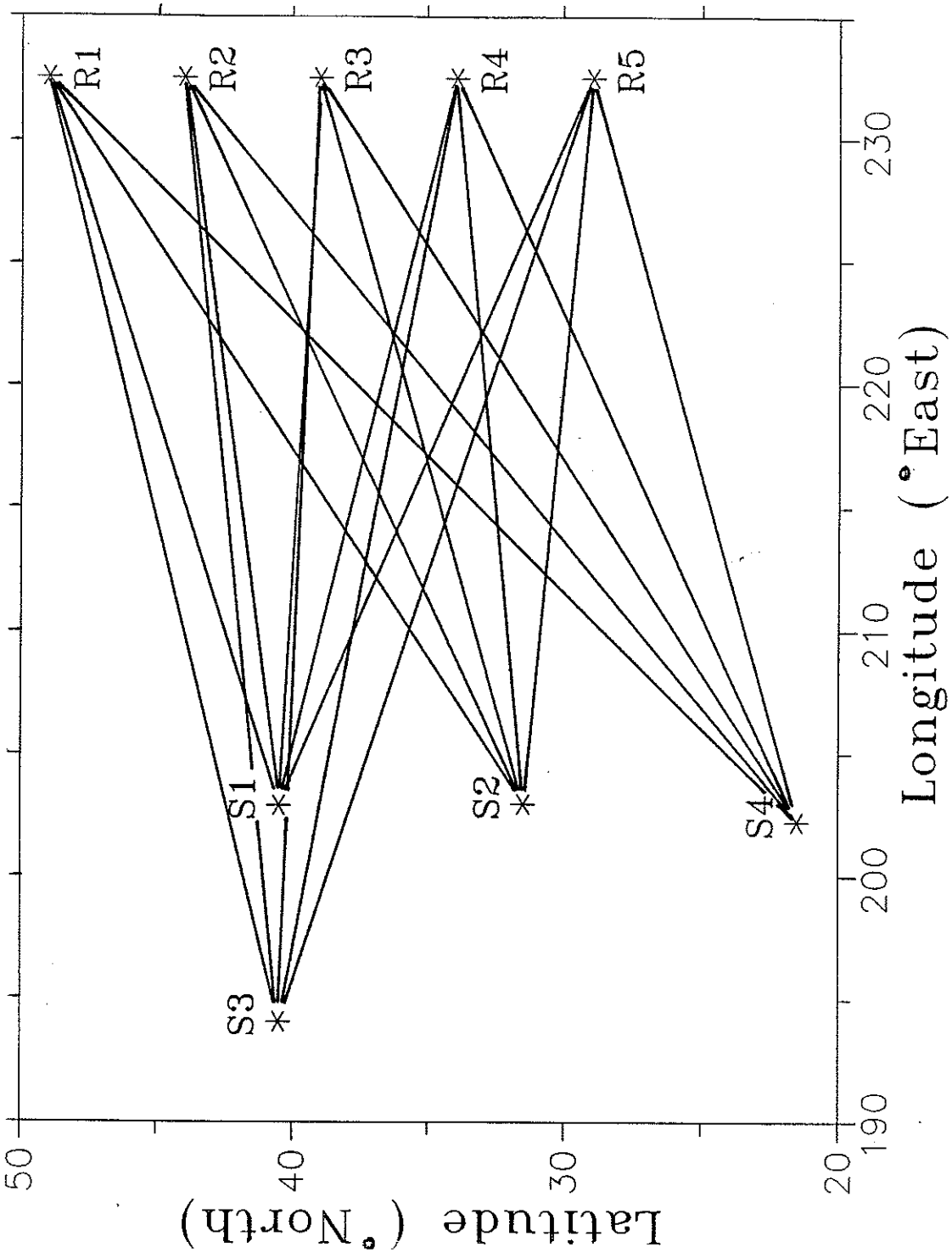

Figure 3.1: The acoustic tomography experiment of 1986-87 consisted of three deep ocean tethered sources (S1-S3), one source (S4) near Kaneohe Bay, Oahu, and about ten receivers, five of which (R) are shown at approximate positions along the West coast of the United States. The area covered by this array was about 4000 km x 3000 km.

current (Munk, Snodgrass, and Wimbush, 1970). Depths and bottom slopes are computed from Schwiderski's "hydrodynamical ocean bathymetry" (Schwiderski, 1978).

The Wiener filter is able to estimate the barotropic current models, a_1, a_2, b_1, and b_2, accurately over large areas (Figures 3.2 and 3.3). Currents in areas approximately 1000 km x 1000 km can be mapped with an error less than 0.01 cm/s.

The *a-priori* variance of the surface displacement can be evaluated using equation (3.4) and the assumptions of equations (3.30) and (3.31) to give,

$$E\left[\eta_0^2\right] = \frac{\sigma^2}{(r\omega)^2}\left[(h_\theta + h\cot\theta)^2 + h_\phi^2 \csc^2\theta + \frac{4h^2}{L^2}\right]. \qquad (3.31)$$

As evident from equation (3.31), the natural (*a-priori*) variability of the surface displacement (Figure 3.4) is closely related to the bottom topography (Figure 3.5). The Wiener filter is able to estimate surface displacements over large areas (approximately 2500 km x 2000 km) to an accuracy greater than 1 cm (Figure 3.6).

The inversion filter is robust in the presence of noise. A travel time uncertainty of 10 ms has minimal effect on the current and surface displacement estimation errors (Figures 3.7, 3.8, and 3.9).

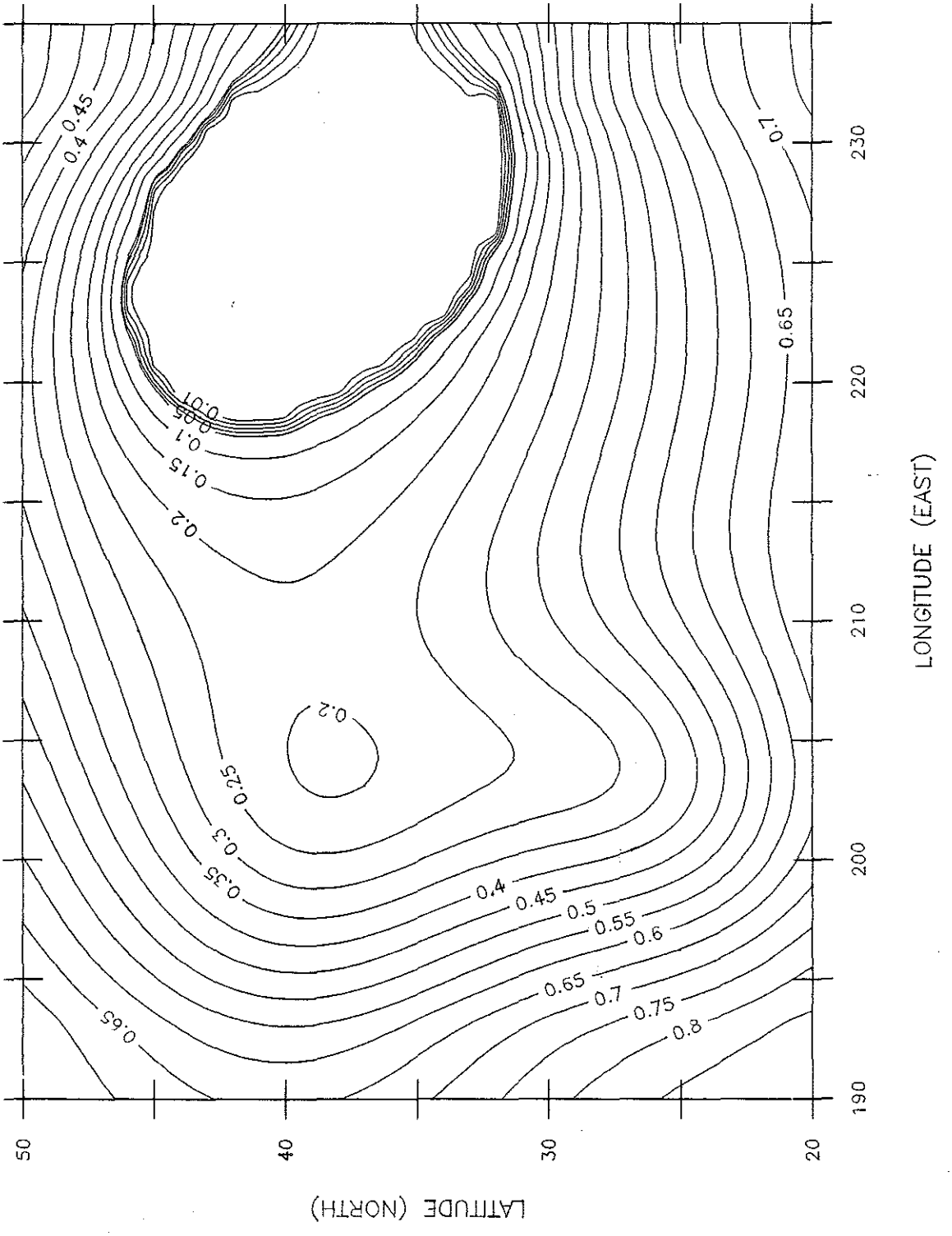

Figure 3.2: Root mean square estimation error (cm/s) of the north/south barotropic current models ($\hat{a_1}$ and $\hat{a_2}$) for a Gaussian decorrelation length of 1500 km and no data noise. An $a - priori$ variance of 1.0 cm^2/s^2 is assumed.

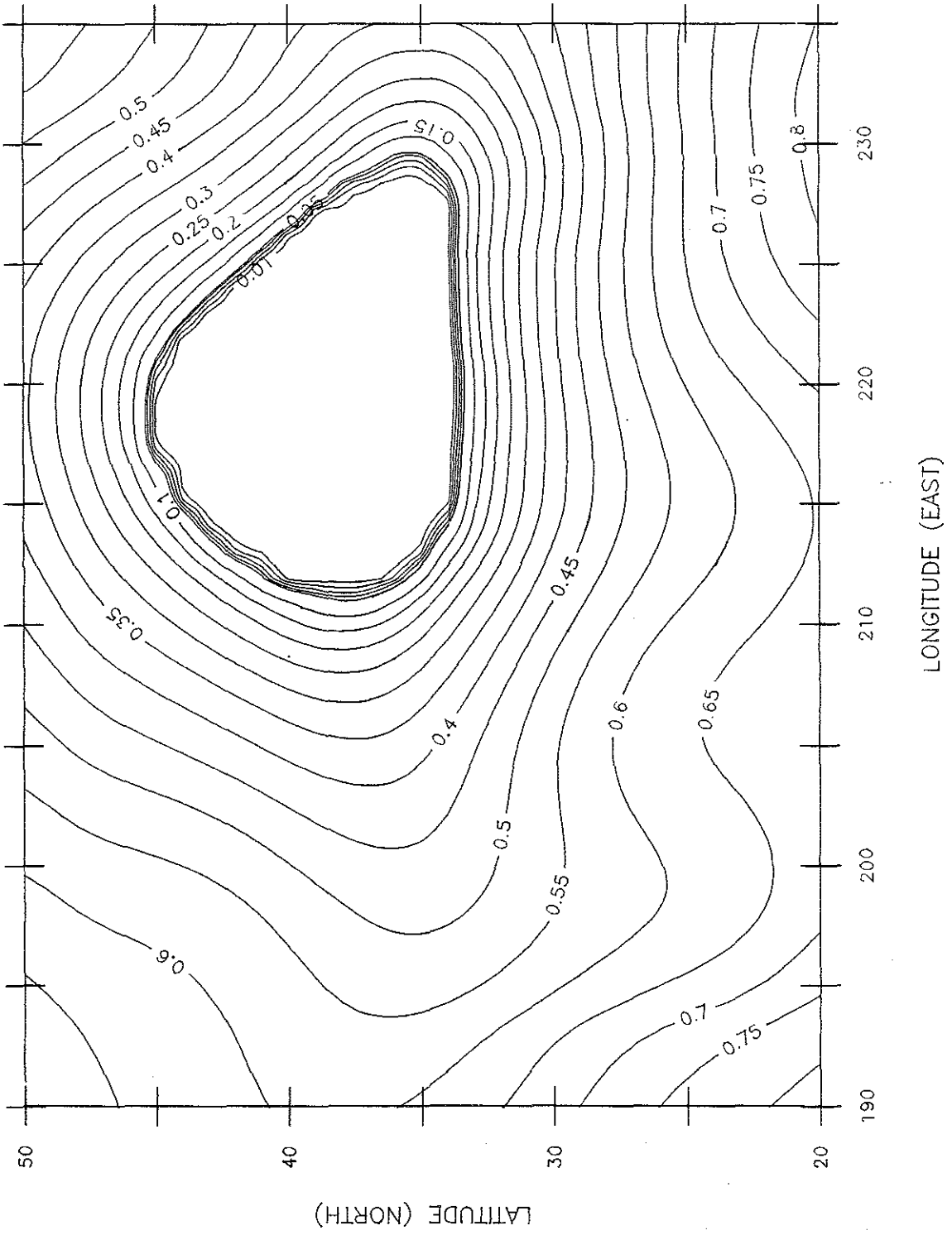

Figure 3.3: Root mean square estimation error (cm/s) of the east/west barotropic current models ($\hat{b_1}$ and $\hat{b_2}$) for a Gaussian decorrelation length of 1500 km and no data noise. An $a - priori$ variance of 1.0 cm^2/s^2 is assumed.

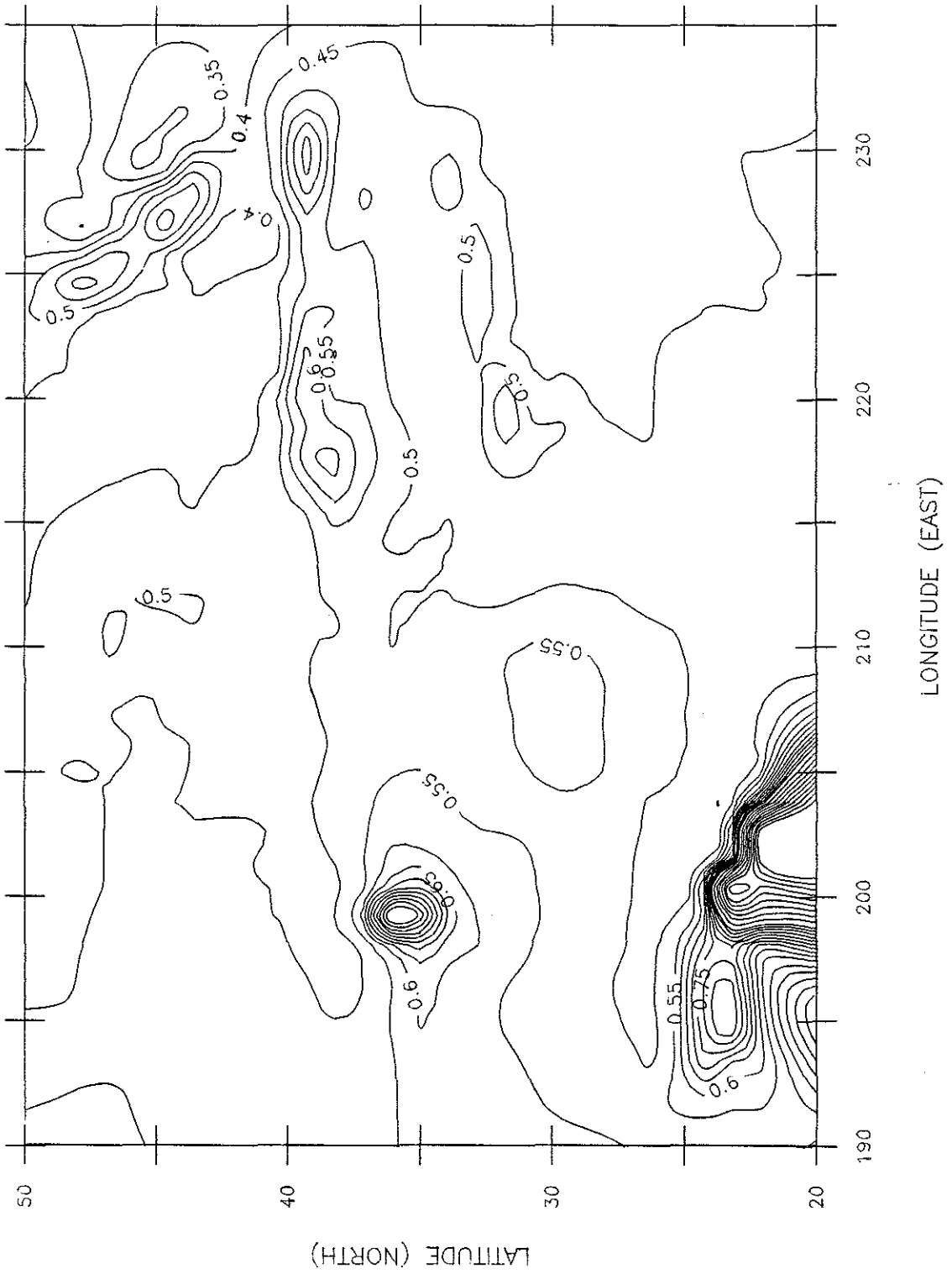

Figure 3.4: Natural variability (m) of the surface displacement (η_0) in the absence of any measurements for a Gaussian decorrelation length of 1500 km. An $a - priori$ variance of 1.0 cm^2/s^2 for each current model (a_1, a_2, b_1, and b_2) is assumed.

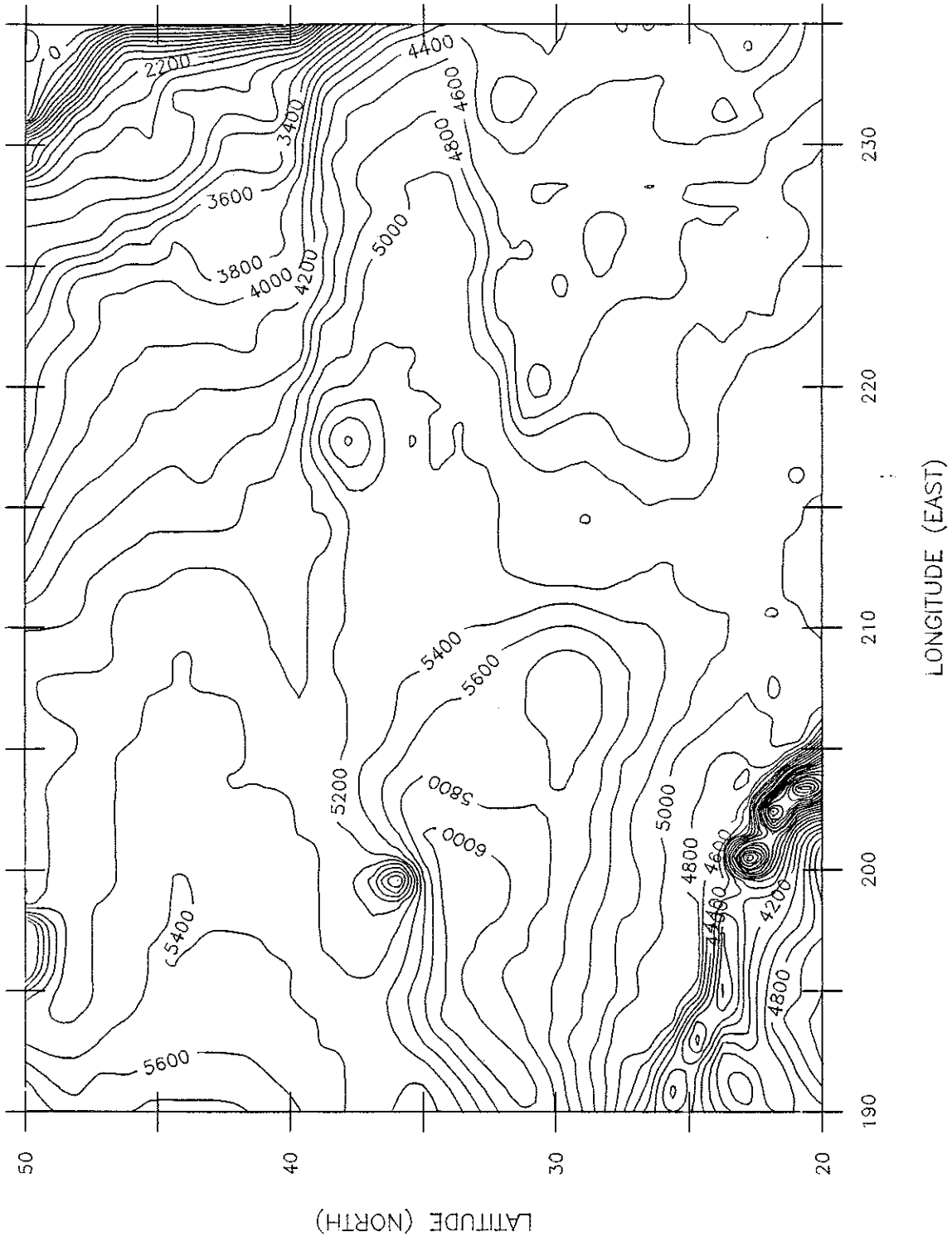

Figure 3.5: Ocean depths (m) for the area covered by the source-receiver array of Figure 3.1. Depth contours are at intervals of 200 m.

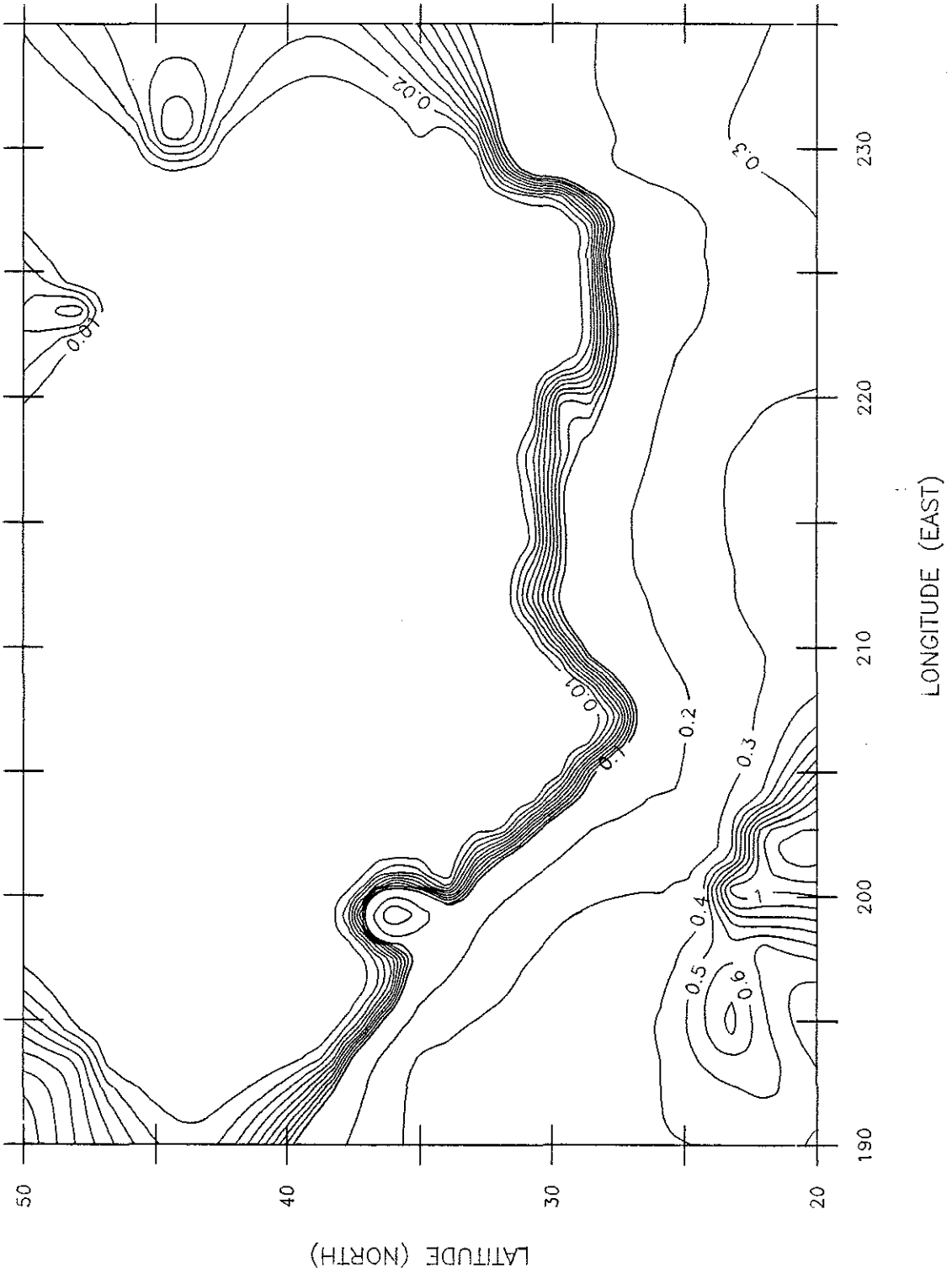

Figure 3.6: Root mean square estimation error (cm/s) of the surface displacement (η_0) for a Gaussian decorrelation length of 1500 km and no data noise. An $a-priori$ variance of 1.0 cm^2/s^2 for each current model (a_1, a_2, b_1, and b_2) is assumed.

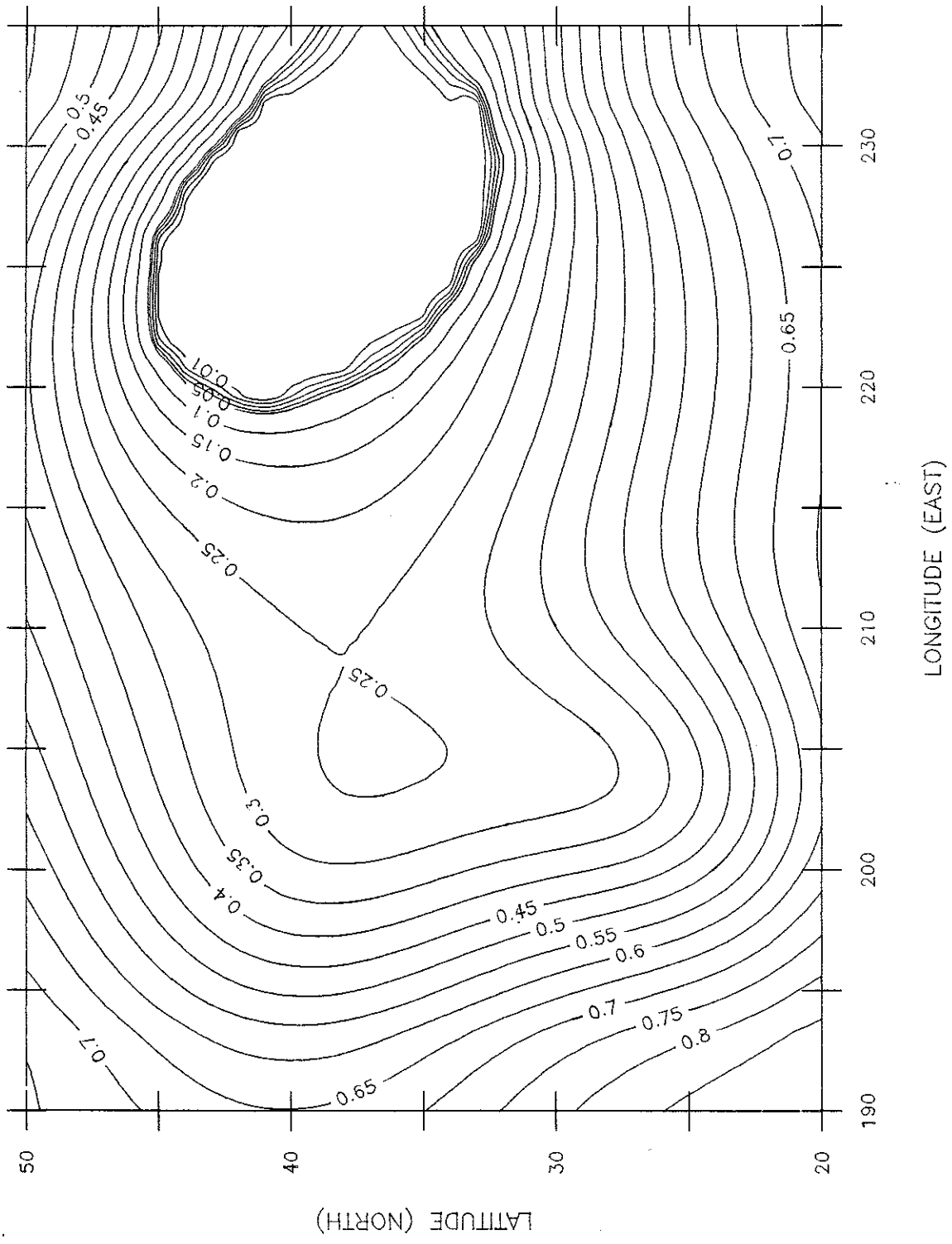

Figure 3.7: Root mean square estimation error (cm/s) of the north/south barotropic current models ($\hat{a_1}$ and $\hat{a_2}$) for a Gaussian decorrelation length of 1500 km and a data noise level of 10 ms. An $a - priori$ variance of 1.0 cm^2/s^2 is assumed.

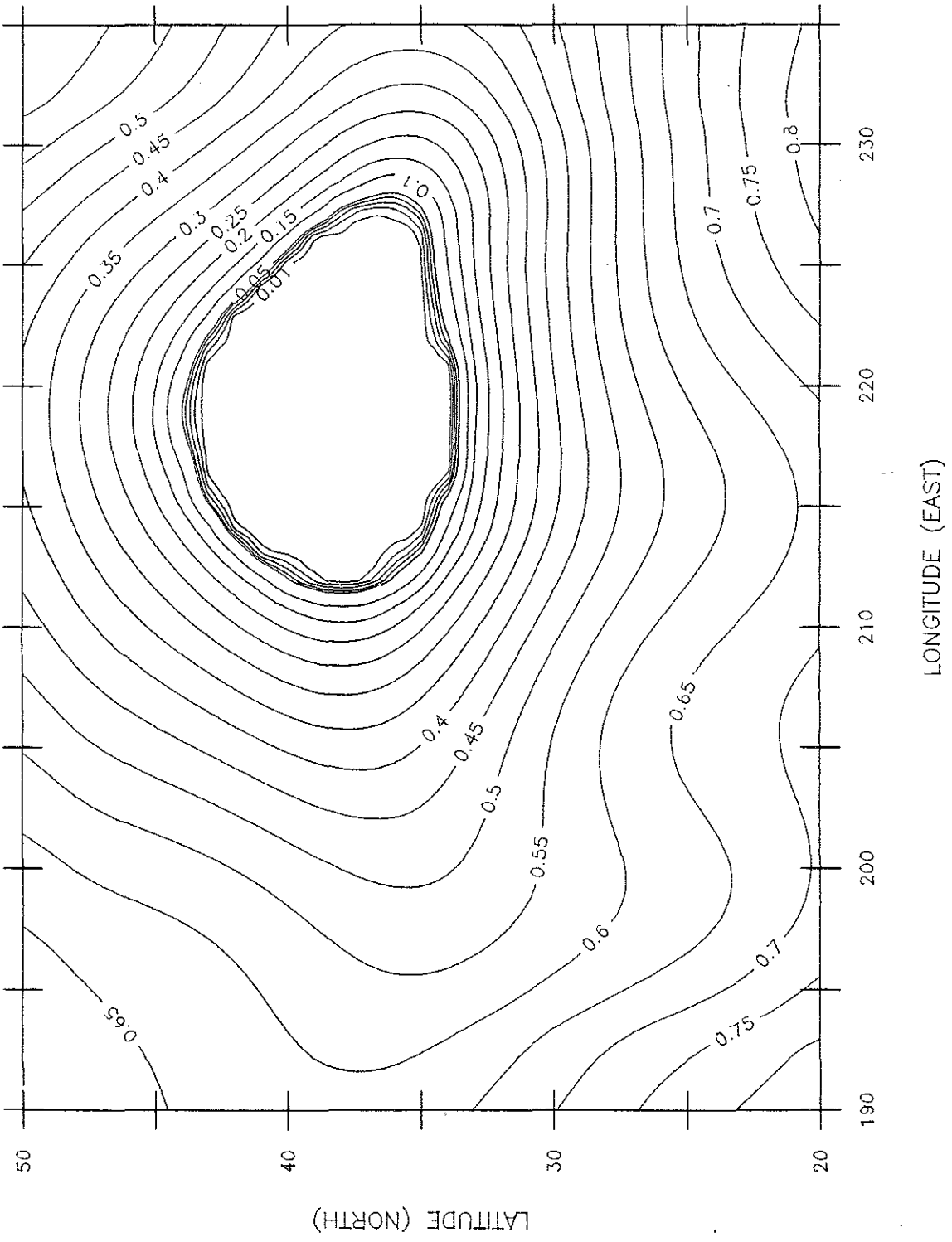

Figure 3.8: Root mean square estimation error (cm/s) of the east/west barotropic current models ($\hat{b_1}$ and $\hat{b_2}$) for a Gaussian decorrelation length of 1500 km and a data noise level of 10 ms. An $a - priori$ variance of 1.0 cm^2/s^2 is assumed.

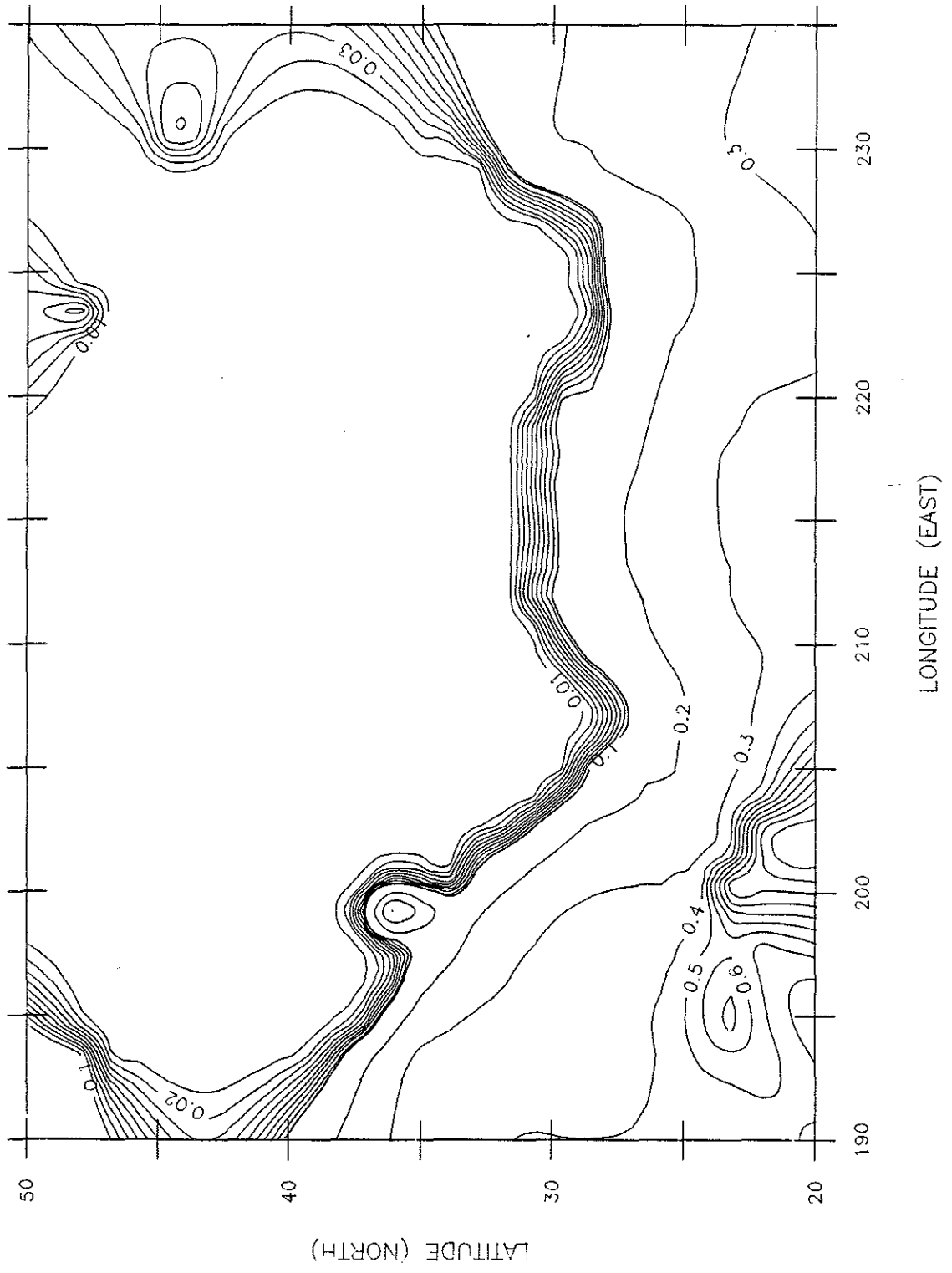

Figure 3.9: Root mean square estimation error (cm/s) of the surface displacement (η_0) for a Gaussian decorrelation length of 1500 km and a data noise level of 10 ms. An $a - priori$ variance of 1.0 cm^2/s^2 for each current model (a_1, a_2, b_1, and b_2) is assumed.

3.4 Conclusions

Movement of the tethered sources results in tomographic travel time changes which must be taken into account when estimating the data, $e_i(\omega)$ and $f_i(\omega)$ (Cornuelle, 1985).

A lack of transmissions for a period exceeding the decorrelation time of the received pulses causes an ambiguity in extending the travel time fluctuation series. The rate of change of the travel time is not ambiguous across transmission gaps. Since the barotropic tides are periodic, the data, $e_i(\omega)$ and $f_i(\omega)$, can be computed from the differentiated travel time series.

The time for sound to travel 4000 km is about 44 minutes. Neglect of the change in currents and surface displacement over this interval introduces significant errors in the estimates (the currents and surface displacement of a semi-diurnal tide can change by as much as 37 percent of their amplitude). Correction is made by including a time delay term (a function of the transmission path and geographic position) in the forward problem.

The inversion filter presented is relatively unconstrained, requiring only conservation of mass and assuming statistical independence of the current models. Application of the momentum equation halves the number of independent models to estimate and reduces the estimation errors with a cost of additional computation. The estimation errors will also be improved by increasing the number of receivers (there were approximately ten in the AT86-87 experiment) (Bushong, Spiesberger, 1987). Bottom pressure gauge data can also be included giving a reduction in error.

The computations required were done in a personal computer on a Definicon Systems DSI-020/780 coprocessor board (4 Mbytes of RAM and equivalent in speed to a VAX-11/780) in about 8 hours.

Bibliography

[1] Aki, K., and P. Richards, "Quantitive Seismology. Theory and Methods, Volume II," Freeman and Co., San Francisco, (1980)

[2] Bushong, P., and J. Spiesberger, "Tomographic maps of the barotropic tides of the Northeast Pacific," in preparation, (1987)

[3] Cornuelle, B., "Inverse methods and results from the 1981 ocean acoustic tomography experiment," Ph.D. thesis, Massachusetts Institute of Technology/Woods Hole Oceanographic Institution, (1983)

[4] Cornuelle, B., "Simulations of acoustic tomography array performance with untracked or drifting sources and receivers," J. Geophys. Res., 90, 9079-9088, (1985)

[5] Estes, R., "A computer software system for the generation of global ocean tides including crustal loading effects," Contract NAS5-20045, Business and Technol. Syst. TR-77-41, (1977)

[6] Kailath, T., "Lectures on Wiener and Kalman Filtering," Springer-Verlag, New York, (1981)

[7] Kay, S. and S. Marple, "Spectrum analysis - A modern perspective," Proc. IEEE, Vol 69, 1380-1419, (1981)

[8] Lamb, H., "Hydrodynamics," 6th ed., Dover, New York, (1932)

[9] Longuet-Higgins, M. and G. Pond, "The free oscillations of fluid on a hemisphere bounded by meridians of longitude," Phil. Trans. Roy. Soc. Lond., A, 266, 193-233, (1970)

[10] Luther, D., "Why haven't you seen an ocean mode lately?," Ocean Modelling, 50, 1-6, (1983)

[11] Marple, S., "Digital Spectral Analysis with Applications," Prentice-Hall, Inc., Englewood Cliffs, N.J., (1987)

[12] Miller, A., "Barotropic planetary-topographic oscillations in ocean basins," Ph.D. Dissertation, University of California, San Diego, (1986)

[13] Munk, W., F. Snodgrass, and M. Wimbush, "Tides off-shore: Transition from California coastal to deep-sea waters," Geophys. Fluid Dyn., 1, 161-235, (1970)

[14] Munk, W., and C. Wunsch, "Ocean acoustic tomography: a scheme for large scale monitoring," Deep-Sea Res. 26a, 123-161, (1979)

[15] Munk, W., B. Zetler, J. Clark, S. Gill, D. Porter, J. Spiesberger, and R. Spindel, "Tidal effects on long-range sound transmission," J. Geophys. Res., 86, 6399-6419, (1981)

[16] Ocean Tomography Group, "A demonstration of ocean acoustic tomography," Nature, 299, 121-125, (1982)

[17] Parke, M., and M. Hendershott, "M2, S2, K1 models of the global ocean tide on an elastic earth," Mar. Geod., 3, 379-408, (1980)

[18] Pedlosky, J., "Geophysical Fluid Dynamics," 2nd ed., Springer-Verlag, New York, (1987)

[19] Platzman, G., "Normal modes of the world ocean. Part I: Design of a finite-element barotropic model," J. Phys. Oceanogr., 8, 323-343, (1978)

[20] Platzman, G., G. Curtis, K. Hansen, and R. Slater, "Normal modes of the world ocean. Part II: Description of modes in the period range 8 to 80 hours," J. Phys. Oceanogr., 11, 579-603, (1981)

[21] Schwiderski, E., "Global ocean tides, Part I: A detailed hydrodynamical interpolation model," NSWC/DL-TR, (1978)

[22] Spiesberger, J., P. Bushong, K. Metzger, and T. Birdsall, "Observations of resonant oscillations in the Northeast Pacific," in preparation, (1987)

[23] Spiesberger, J., K. Metzger, and T. Birdsall, "A basin scale ocean acoustic tomography experiment in the Northeast Pacific," in preparation, (1987)

[24] Spiesberger, J., R. Spindel, and K. Metzger, "Stability and identification of ocean acoustic multipaths," J. Acoust. Soc. Am. 67, 2011-2017, (1980)

[25] Spindel, R., "An underwater acoustic pulse compression system," IEEE, Vol. ASSP-27, 723-728, (1979)

[26] Van Trees, H., "Detection, Estimation, and Modulation Theory. Part I: Detection, Estimation, and Linear Modulation Theory," Wiley and Sons, New York, (1968)